Chapter 6

DYNAMICAL MODELS OF COROTATING WIND STRUCTURE

In spiral routes by long detours,
(As a much-tacking ship upon the sea,)
For it the partial to the permanent flowing,
For it the real to the ideal tends.

Walt Whitman, *Song of the Universal*

The ubiquitous temporal and structural variability of hot-star winds has been reviewed in Section 1.2.3 above, and in this Chapter we begin to construct hydrodynamical models designed to produce discrete absorption components (DACs) in P Cygni line profiles. As opposed to earlier *kinematic* models of corotating wind structure, the principal goal of this Chapter is to model the *dynamical* effect of radiative driving on the formation of CIRs in a hot star wind, and to compute synthetic observational diagnostics to see if, e.g., slow DAC-like signatures can be theoretically produced. Our computational approach is to apply a reasonable parameterization for a localized "star spot" perturbation in the radiation force near the stellar surface, and allow the wind to respond consistently. Although the actual photospheric structure perturbing the base of the wind is likely to be different, we suspect the characteristic response of a radiatively-driven medium will be insensitive to the details of this physical mechanism, and mainly depend on base changes in the fluid velocity and density.

The remainder of this Chapter is organized as follows (see Cranmer & Owocki 1996). We first (Section 6.1) describe the azimuthally-dependent force enhancement that is utilized to induce nonaxisymmetric structure in the equatorial plane. Next (Section 6.2) we present results for a series of O star models with varying rotation

rates and wind parameters, and discuss the emergent corotating structure. We then (Section 6.3) compute synthetic ultraviolet P Cygni line profile time series for the various models in our parameter study. We also present a representative calculation of the continuum polarization variations for one of these models with time and observer-inclination. Finally, a discussion and conclusion section (Section 6.4) summarizes our results and outlines directions for future work.

6.1 The Local Radiative Force Enhancement

We induce azimuthal structure in our models by varying the Sobolev line force over a localized "star spot" in the lower wind. Since this force is directly proportional to the stellar flux ($L_*/4\pi r^2$), increasing or decreasing $g_r^{\rm lines}$ over a small area is operationally equivalent to assuming a bright or dark region of the photosphere. Note, however, that by modulating the radiative force in this manner we do *not* mean to literally propose the existence of strong flux-varying spots on early-type stars. We merely use this simple method to perturb the wind in lieu of more definite knowledge about the physical cause(s) of surface inhomogeneities. Because the line driving grows weaker as one moves deeper into the subsonic wind and photosphere, the force enhancement is essentially confined to the transonic and supersonic wind, obviating the need to model a perturbed stellar atmosphere.

The induced variation in the line force is assumed to have a specified radial and azimuthal dependence which remains fixed to the stellar surface, and thus rotates through the computational domain with the star. The force enhancement is a function of radius r and a corotating azimuthal angle ψ,

$$\psi \;=\; \phi - \Omega t \quad , \tag{6.1}$$

with $\Omega \equiv V_{\rm eq}/R_*$ the star's constant rotational angular velocity. The perturbed line force has the form

$$\begin{aligned} g_r^{\rm lines}(r,\psi) &= g_0(r) + \delta g(r,\psi) \\ &= g_0(r)\left\{1 + A\,\gamma(r)\exp\left[-\left(\psi-\psi_0\right)^2/\sigma^2\right]\right\} \quad , \end{aligned} \tag{6.2}$$

where g_0 is the unperturbed Sobolev force (eq. [2.88]), ψ_0 is the azimuthal position of the center of the spot, and A is its dimensionless amplitude. We will refer to "dark spots" as those with $-1 < A < 0$ and "bright spots" as those with $A > 0$. The azimuthal variation of the force is here assumed to be Gaussian about ψ_0, with full width at half maximum (FWHM) given by $\Phi \equiv 2\sigma\sqrt{\ln 2}$. The radial modulation $\gamma(r)$ is constrained by the geometrical extent of the spot. Close to the star, the spot is all that can be seen, and so $\gamma(r \to R_*) \to 1$; far from the star, the spot only represents a fraction of the observed stellar disk, and so $\gamma(r)$ approaches a small, but constant value as $r \to \infty$.

For a field point directly over ($\psi = \psi_0$) a *circular* flux enhancement with angular diameter Φ, the radial function $\gamma(r)$ can be derived analytically from the the normalized residual flux,

$$\frac{\mathcal{F} - \mathcal{F}_0}{\mathcal{F}_0} \;=\; A\frac{r^2}{R_*^2}\int\!\!\int D(r,\mu',\phi')\,\mu' d\mu' d\phi' \;=\; A\gamma(r) \quad , \tag{6.3}$$

where $\mathcal{F}$ and $\mathcal{F}_0$ are the total and unperturbed fluxes. The amplitude A takes into account the relative magnitude of the spot's "residual effective temperature," and is equivalent to $(T_{\rm spot}^4 - T_0^4)/T_0^4$. The area integral is taken over a solid angle centered about the z-axis, with angles $\theta' = \cos^{-1}\mu'$ and ϕ' measured from the field point in the wind at radius r, and the residual limb darkening function D set to zero for rays not intercepting the spot. Thus, for simple linear limb darkening,

$$\gamma(r) \;=\; \frac{2\pi r^2}{R_*^2}\int_{\mu_0(r)}^1 \frac{1}{4\pi}\left(2 + 3\sqrt{\frac{\mu'^2 - \mu_*^2}{1-\mu_*^2}}\right)\mu' d\mu' \quad , \tag{6.4}$$

where $\mu_* \equiv [1 - (R_*^2/r^2)]^{1/2}$ defines the stellar limb, and

$$\mu_0(r) \;=\; \begin{cases} \mu_*, & r\cos(\Phi/2) \le R_* \\ \sqrt{1 - R_*^2\sin^2(\Phi/2)/S^2}, & r\cos(\Phi/2) > R_* \end{cases} \tag{6.5}$$

defines the visible edge of the spot. The distance S from the field point to the edge of the spot is $[r^2 + R_*^2 - 2rR_*\cos(\Phi/2)]^{1/2}$. We thus adopt the radial modulation function given by the analytic integral of (6.4),

$$\gamma(r) \;=\; \frac{1}{2}\left[1 + \left(\frac{1-\mu_0^2}{1-\mu_*^2}\right) - \left(\frac{\mu_0^2 - \mu_*^2}{1-\mu_*^2}\right)^{3/2}\right] \quad , \tag{6.6}$$

which approaches unity as $r \to R_*$ and approaches a constant value of $[1+\sin^2(\Phi/2) - \cos^3(\Phi/2)]/2$ as $r \to \infty$. Although this residual flux integral is also able to provide oblique ($\psi \neq \psi_0$) and nonradial components of the flux enhancement of a star spot, we restrict our present models to the explicit *radial* perturbation given by equations (6.2) and (6.6).

Again we emphasize that we do not intend here to propose that bright or dark spots are necessarily the specific mechanism for inducing corotating stream structure in hot-star winds. (Indeed, we intend our results to provide a more generic representation of the wind response to a large variety of base perturbations, including, e.g., magnetic fields, nonradial pulsations, or mass ejections.) Taken literally, the standard spot models here, with $A = \pm 0.5$ and $\Phi = 20°$, should produce observable photometric variations at the 1–2% level. But other weaker and smaller spot

models we have computed (see Figures 6.16 and 6.17) can also yield visible DAC wind structure with a much lower, perhaps undetectable, photometric signature.

Figure 6.1 shows contours of the force enhancement in the equatorial plane for a spot with $\Phi = 20°$, as well as wind "streaklines" for various stellar rotation speeds, as discussed further below (Section 6.2.3). Note that the spot significantly affects only a relatively small area of the wind: an azimuthal extent of $\sim 2\Phi$ and a radial extent of about a stellar radius. This allows several spots to be superposed on the stellar surface without any appreciable overlap in their force enhancements. Following the empirical arguments of Kaper & Henrichs (1994), who suggest a variable dipole magnetic field as the seed of large-scale wind structure, we place *two* spots separated by 180° on our model stars.

Before examining how a rotating wind responds to the localized force enhancement, it is instructive to see how a non-rotating wind is affected. Figure 6.2 shows the radial velocity and density (directly over the spot) at a reference radius of $10R_*$, well beyond the region of significant direct force enhancement, as a function of amplitude A. The general trend is for a "bright" spot to increase the local mass loss and thus increase the density of the wind near the star. Further out in the wind, where the effect of the spot drops off, the radiative force cannot accelerate the higher density material as strongly, so it approaches a *lower* terminal speed than in the unperturbed wind. Conversely, "dark" spots decrease the mass loss in the surrounding wind and thus allow the less dense material to be accelerated more strongly, leading to a much *higher* terminal speed. The three sets of data in Figure 6.2 correspond to: (1) one-dimensional, finite-disk, "modified CAK" (mCAK) solutions with a realistic critical point analysis (solid lines), (2) numerical two-dimensional hydrodynamical models using VH-1 (filled circles), and (3) a simple analytic fit to the data (dashed lines). The one-dimensional mCAK models contain the radial spot modulation $\gamma(r)$, but no information about neighboring streamline divergence or convergence. For spots with $A \gtrsim 0.6$, the one-dimensional models cease to have steady-state solutions that reach to infinity because too much mass is driven off the star to be accelerated beyond its gravitational escape velocity. The two-dimensional models can drive more mass to infinity because the density is reduced by a slight azimuthal expansion, which leads to a faster-than-radial divergence of flow tubes (see, e.g., MacGregor 1988).

The simple fit to the velocity and density variation in Figure 6.2 depends on only one free parameter, and makes use of the approximate dependence of the CAK mass loss rate on an arbitrary force multiplier (see Cranmer & Owocki 1995, eq. [24]). Directly over the spot,

$$\dot{M} \approx \dot{M}^{(0)}(1+A)^{1/\alpha} \ , \tag{6.7}$$

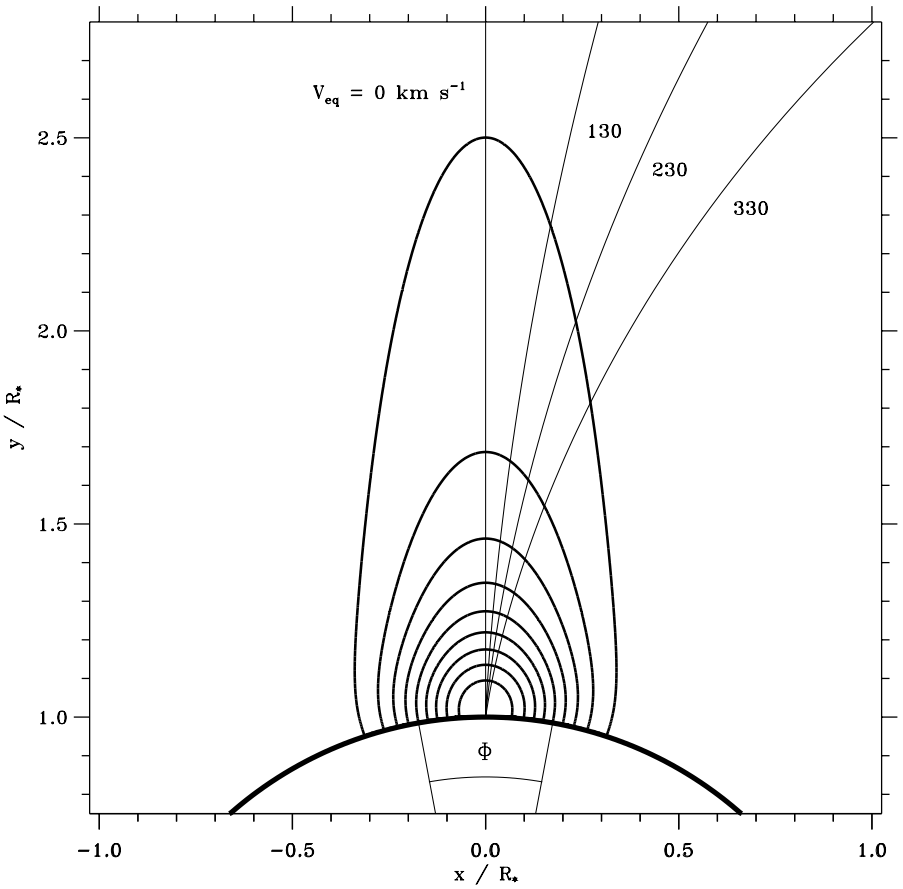

Figure 6.1: Contours of the star-spot force enhancement for a spot with full width at half maximum $\Phi = 20$ degrees. The contour levels shown range from $0.1A$ to $0.9A$ in intervals of $0.1A$. Overplotted are streaklines of unperturbed wind models from stars rotating at 0, 130, 230, and 330 km/s.

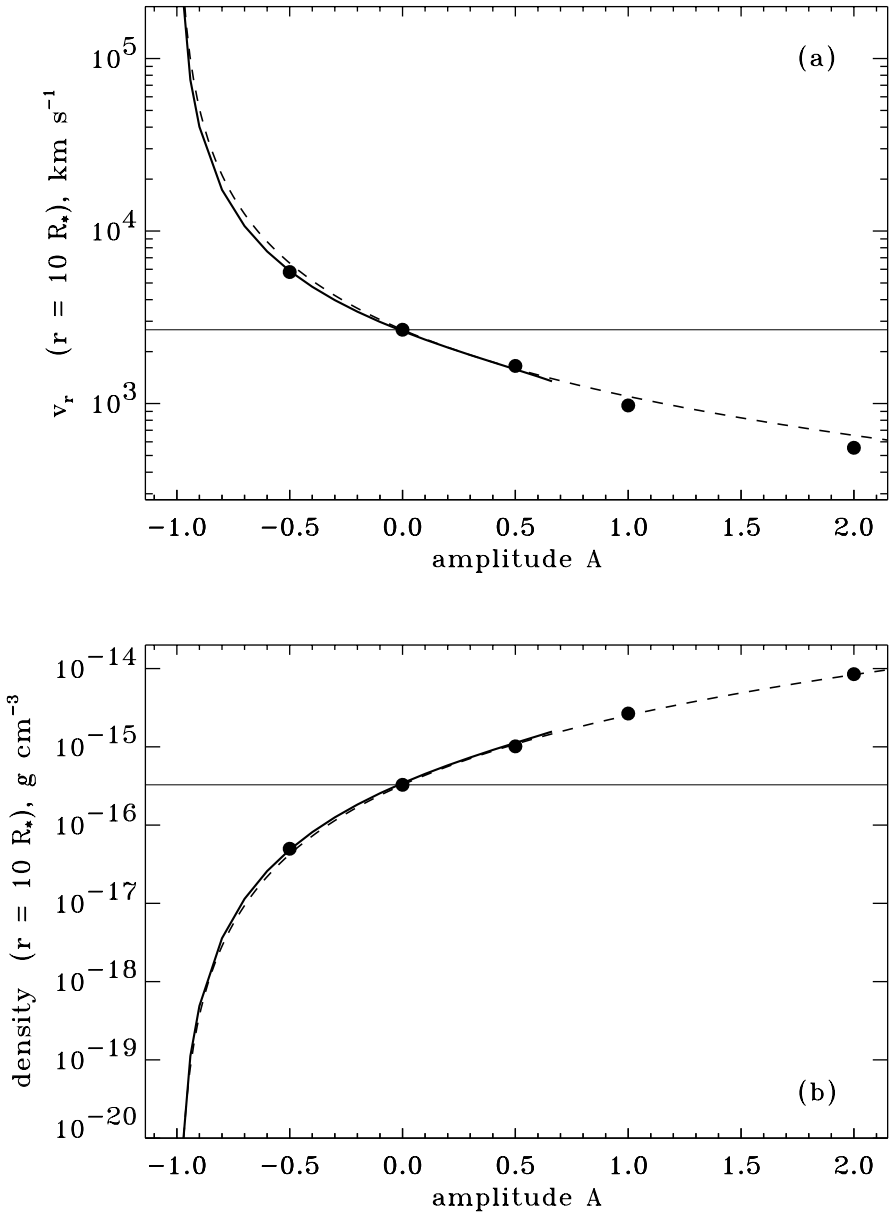

Figure 6.2: Variation with spot amplitude (for $\Phi = 20$ degrees) of (a) radial velocity and (b) density at a radius of 10 stellar radii, for non-rotating winds. Solid lines show one-dimensional mCAK solutions, filled circles show two-dimensional hydrodynamical solutions, and dashed lines show a simple one-parameter fit to both sets of data.

where $\dot{M}^{(0)}$ is the unperturbed mass loss rate, and we assume that the CAK critical point r_c, where the mass flux is determined, is close enough to the star that $\gamma(r_c) \approx 1$. In a one-dimensional steady state, the mass conservation equation is integrated in the usual way to obtain $\dot{M} = 4\pi\rho v_r r^2$, and this provides a relation between the velocity and density at a given radius. We thus define fitting functions which obey this multiplicative constraint:

$$\rho \approx \rho^{(0)}(1+A)^{s/\alpha} \quad , \tag{6.8}$$

$$v_r \approx v_r^{(0)}(1+A)^{(1-s)/\alpha} \quad , \tag{6.9}$$

where we have found the best fit value of $s = 1.77$ for our dashed-line fits in Figure 6.2.

6.2 Numerical Results

Because the DAC phenomenon is primarily observed in O-star winds, we choose to center our study on a standard model of the O4f supergiant ζ Puppis. Specifically, we take $M_* = 60 M_\odot$, $R_* = 19 R_\odot$, $L_* = 8 \times 10^5 L_\odot$, and $T_{\rm eff} = 42,000\,{\rm K}$ (see, e.g., Howarth & Prinja 1989; Kudritzki et al. 1992). The measured rotational $V_{\rm eq} \sin i$ for ζ Puppis is 230 km s^{-1}, which we take for the equatorial rotation velocity of our standard model. We neglect the small ($\sim$7%) oblateness induced by this degree of rotation, which corresponds to a Roche equipotential surface rotating at 63% of its critical angular velocity. We assume an isothermal wind of temperature $T_{\rm eff}$, corresponding to a sound speed $a = 24\,{\rm km\ s^{-1}}$, and use the line-driving constants $\alpha = 0.60$ and $k = 0.15$ (see eq. [2.88]). In one-dimensional mCAK models, these result in a terminal velocity $v_\infty = 2580\,{\rm km\ s^{-1}}$ and a mass flux $\dot{M} = 3.28 \times 10^{-6}\, M_\odot/{\rm yr}$. We use the VH-1 hydrodynamics code described above in Section 2.3.3, and model the wind in the equatorial plane, varying r (from R_* $30R_*$) and ϕ (from 0° to 180°) on the two-dimensional computational grid (Cranmer & Owocki 1996).

The Sobolev approximation assumes a monotonically accelerating velocity field, but this is not guaranteed in the time-dependent simulations presented below. Winds with nonmonotonic velocities have *nonlocal* line forces, since multiple resonance surfaces can create additional attenuation of the stellar flux (Rybicki & Hummer 1978; POF). We do not treat this nonlocal coupling directly, but we have compared CIR models using an upper limit (unattenuated) and a lower limit (strongly attenuated) for the line force in multiply-resonant regions of the wind. The lower limit assumes decelerating flows ($\partial v_r/\partial r < 0$) receive the same small force contribution from nonradial rays as a flow that is not accelerating at all ($\partial v_r/\partial r = 0$). The upper limit uses the absolute value of the radial velocity gradient $|\partial v_r/\partial r|$ in equation (2.88) and in the finite disk factor f. In practice, we find the overall wind

dynamics to be qualitatively similar in both limits, but have standardized on the upper limit method for all the results presented here.

The localized "star spot" radiative force enhancement described above depends primarily on two quantities: the amplitude A and the azimuthal full width Φ. These, together with the equatorial rotation velocity $V_{\rm eq}$, are the three free parameters we vary in our study of non-axisymmetric structure formation. Table 6.1 outlines the input parameters and several output quantities (to be discussed below) for the models we computed. Models 1 and 2 are standard "bright" and "dark" spot models, with $A = +0.5$ and -0.5, and they represent a basis to explain the general hydrodynamical phenomenon of stream interaction. The subsequent models in Table 6.1 are intended to confirm our understanding of the physics of CIR formation, and are discussed below in a more limited fashion. In Table 6.1 we also define Δv_r as the maximum absolute velocity perturbation $(v_r - v_r^{(0)})$ in the model, either positive or negative, and the other variables are discussed further below. All velocities in Table 6.1 are expressed in km s^{-1}.

6.2.1 Standard Bright Spot: Model 1

Figure 6.3 shows gray-scale plots for the density, radial velocity, azimuthal velocity, and radial Sobolev optical depth in Model 1, *normalized to the unperturbed wind*. To ease comparison with other models, the azimuthal coordinates here have been incremented by a constant factor to align the peak of the spot (ψ_0) with the center-line or x-axis of the diagram. Note the expected tendency for a bright spot to create higher density and lower radial velocity. However, the *azimuthal* velocity only differs by a small subsonic amount from the unperturbed angular-momentum-conserving form $v_\phi^{(0)}(r) = V_{\rm eq} R_*/r$. This demonstrates the almost purely *radial* effect of the spot enhancement.

Most of the corotating structure from the spot settles onto nearly constant spiral "streaklines" in the wind. In the present models, streaklines are equivalent to flow streamlines in the star's rotating frame of reference. Figure 6.4 compares streamlines and streaklines computed for Model 1. By numerically integrating the kinematic relation

$$\frac{r\, d\phi}{dr} = \frac{v_\phi(r,\phi) - r\Omega_F}{v_r(r,\phi)} \quad , \tag{6.10}$$

from a locus of points on the stellar surface spaced evenly in ϕ, one can alternatively compute either streamlines in the inertial reference frame, with $\Omega_F = 0$, or streaklines in the rotating reference frame, with $\Omega_F = \Omega$. Areas with a higher (lower) concentration of streaklines correspond to regions of relative compression (rarefaction), though not all density variations are reflected in the streaklines. The dashed lines in Figure 6.4 show the streamline and streakline originating directly over the

Table 6.1: Summary of CIR Parameter Study

Model	A	Φ	$V_{\rm eq}$	$(\rho/\rho^0)_{\rm max}$	Δv_r	r_L/R_*	r_{NL}/R_*	r_i/R_*
1	+0.50	20°	230	3.747	–629.2	1.607	6.417	6.736
2	–0.50	20°	230	5.071	+2272.	2.188	—	7.646
3A	+0.01	20°	230	1.023	–29.30	8.169	6.005	306.0
3B	+0.10	20°	230	1.243	–193.0	2.782	6.157	31.10
3C	+2.50	20°	230	39.95	–1285.	1.210	6.157	1.981
4A	+0.50	10°	230	2.840	–598.3	1.163	3.736	3.868
4B	+0.50	40°	230	2.206	–493.3	2.526	10.38	12.47
4C	+0.50	80°	230	1.977	–238.8	4.383	>30	23.94
5A	+0.50	20°	130	3.969	–783.4	1.892	9.324	11.90
5B	+0.50	20°	330	2.485	–482.9	1.492	4.934	4.556

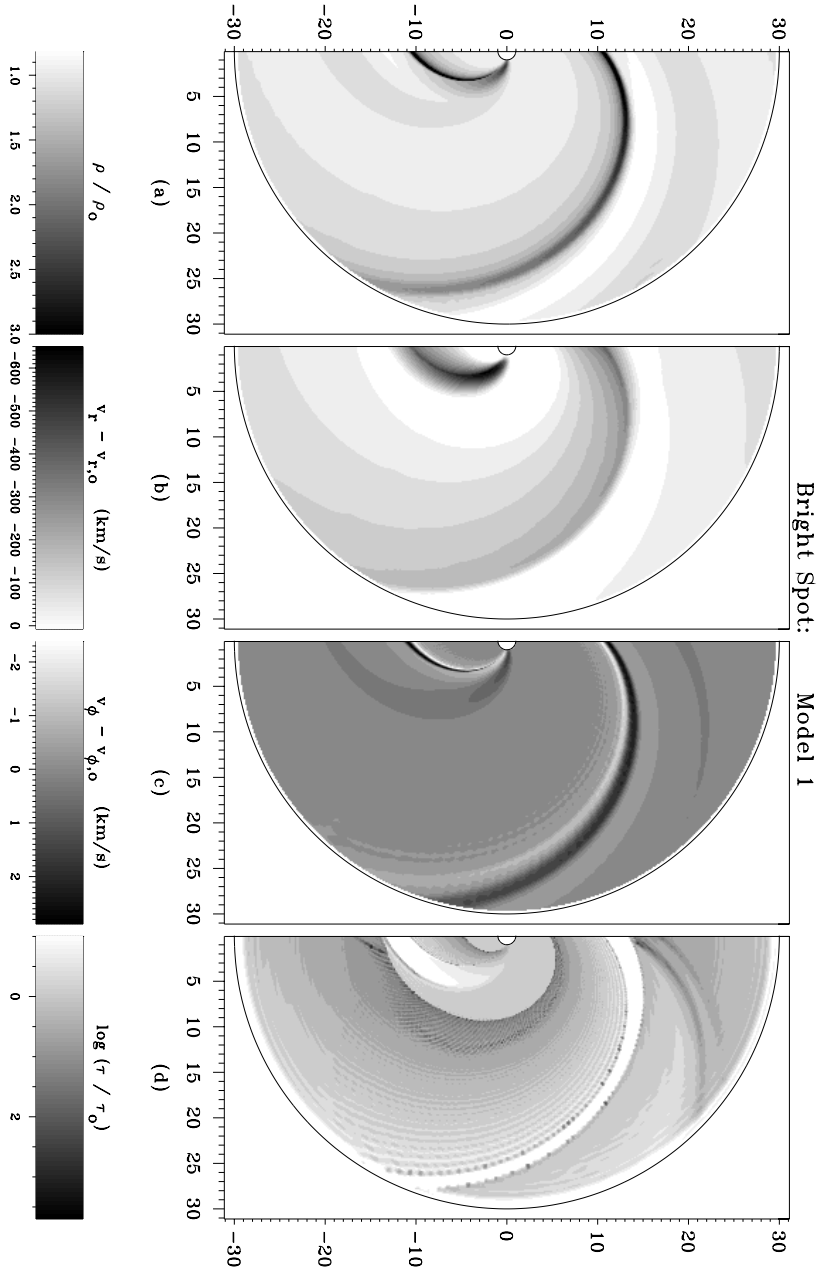

Figure 6.3: CIR structure for Model 1, settled to a steady state. Shown are the (a) density, (b) radial velocity, (c) azimuthal velocity, and (d) radial Sobolev optical depth, all normalized to the unperturbed wind initial condition.

spot. The streamline appears nearly radial, but careful inspection shows that it has a modest (18°) prograde deflection, resulting from corotation of the relatively slow wind outflow near the surface. Through most of the wind, however, the streamlines are close to radial, and this allows one to qualitatively interpret the azimuthal coordinate as a *time* dimension. For any streamline at a fixed value of ϕ, which is intercepted by different streaklines as the (corotating steady state) system sweeps by, the two-dimensional hydrodynamics becomes effectively one-dimensional, but now truly time dependent. This concept allows us to understand the "spread out" CIR structure in terms of a simpler model of radial wave or shock propagation. Hundhausen (1973) modeled solar-wind CIR formation and evolution in one dimension using this approximation.

We can disentangle the actual patterns of high density, low velocity, and more optically thick CIR structure by examining several causally-connected regions of this model:

I. **Direct Enhancement:** Close to the stellar surface, the Gaussian-shaped spot increases the mass flux and wind density over a limited ($r \lesssim 2R_*$) region near the star. This enhanced-density patch is slightly deformed by rotation from the contours shown in Figure 6.1, but is essentially equivalent. The density increases over the spot by a maximum factor of ~2.6, only slightly smaller than that predicted by the non-rotating analysis (see eq. [6.8]). This region also shows considerable azimuthal spreading in v_ϕ as the wind begins to adjust to the presence of the spot.

II. **Prograde Precursor:** Just ahead of the spot ($\psi > \psi_0$), a small fraction of the enhanced higher-density wind is able to "leak out" azimuthally and settle onto a set of relatively unperturbed streaklines. The density in this feature is only enhanced by a factor of ~1.2, indicating that it comes from material in the prograde tail of the Gaussian distribution. It becomes isolated from the direct spot enhancement at a relatively large distance from the star ($r \approx 6.4R_*$) after the CIR rarefaction (IV) has appeared between it and the CIR shock (III).

III. **CIR Compression:** The low radial velocity wind from the center of the spot curls around on more tightly-wound streaklines than the surrounding unperturbed wind, and these streams begin to interact at a finite radius from the star ($r \approx 1.6R_*$). Alternately, in the above one-dimensional interpretation, the slow stream can be considered equivalent to a radially-extended Gaussian "wave packet" which nonlinearly steepens as the fast mean wind begins to overtake it. The result of this collision of fast and slow streams is a corotating weak shock compression (the CIR) which, because it is driven by ram pressure from the mainly unperturbed wind, propagates out at very near the

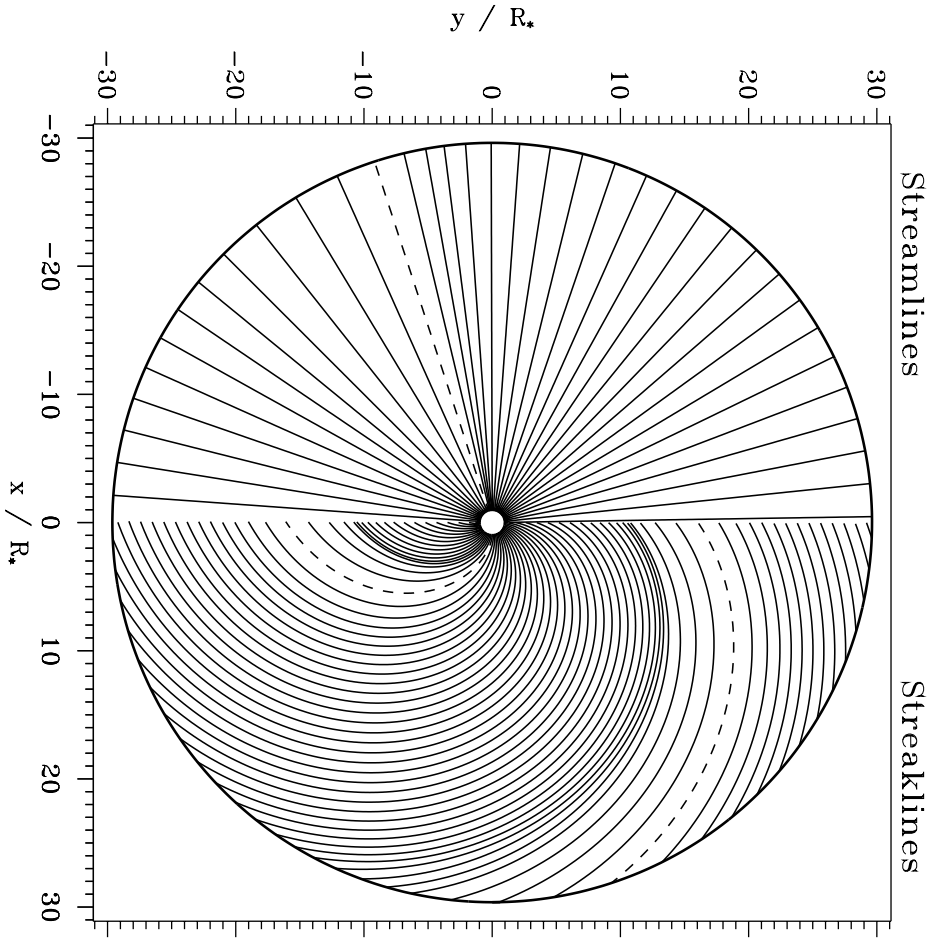

Figure 6.4: Streamlines (left) and streaklines (right) for Model 1, integrated from 72 equally-spaced points on the star, separated by 5 degree intervals. Dashed lines indicate initial points situated at the center of the spot enhancement.

unperturbed wind velocity. Because the flow is isothermal, we do not see a separation into a distinct forward and reverse shock pair, as is observed in the more nearly adiabatic solar wind.

IV. **CIR Rarefaction:** Ahead of the nonlinear shock the streaklines fan out and form a lower-density rarefied region. The formation of this rarefaction is mandated by mass flux conservation, and the radial velocity correspondingly peaks slightly above its unperturbed value here. Because the density in this feature never dips too far below the unperturbed density ($\min[\rho/\rho^{(0)}] \approx 0.82$), the rarefaction propagates out at nearly the same velocity as the CIR compression.

V. **Radiative-Acoustic "Kink:"** In a purely hydrodynamical wind, the radial CIR shock structure is the sole result of the nonlinear steepening of the initial enhancement. Any nondissipative signals propagating in the rest frame of the wind (at characteristic speeds $\pm a$) are limited to the relatively undisturbed lateral (nonradial) direction. In a line-driven wind, however, Abbott (1980) and Rybicki et al. (1990) found that large spatial-scale linear perturbations propagate in the radial direction at modified "radiative-acoustic" characteristic speeds. Abbott (1980) derived

$$C_{\pm} \;=\; -\tfrac{1}{2}U \pm \sqrt{\left(\tfrac{1}{2}U\right)^2 + a^2} \tag{6.11}$$

for radial modes, where $U \equiv \partial(g_r^{\rm lines})/\partial(\partial v_r/\partial r)$ and $C_{\pm}$ reduces to the purely acoustic case if $U = 0$ (see Section 7.2.7 for a full derivation). In most of the wind, though, $U \gg a$, and the outward (positive root) solutions are subsonic, and the inward (negative root) solutions are supersonic. In Model 1 we see both an acoustic lateral mode (spreading in v_ϕ at large radii; Figure 6.3c) and a nonlinear analog of the inward radiative-acoustic mode, which propagates slowly outward in the star's frame ($0 < v_r + C_- < v_r$) as a weak discontinuity, or "kink," in the radial velocity gradient. Because of its slow propagation (more tightly-wound streaklines) this feature eventually collides with the CIR rarefaction from the other spot at a radius of $\sim$13.5 R_* and ceases to exist.

We trace these five features in Figure 6.5, which is a close-up of the density gray-scale shown in Figure 6.3a. Unique tracks were found by searching for local extrema (in radius) of various quantities, and following contiguous patterns around in azimuth. The direct spot enhancement (I) appears at the stellar surface as a local maximum in the normalized density $\rho/\rho^{(0)}$, and collides with the CIR/kink pair of features (III and V) at a radius of $\sim 3.9 R_*$. These "bifurcated" extrema are found by tracking local minima and maxima in the radial velocity, as shown in Figure 6.6 below. They appear at a relatively small radius r_L (see Table 6.1),

where the spot perturbation is still linear. The remaining precursor/rarefaction pair of features (II and IV) correspond to other local minima and maxima in the normalized density, and they appear further out (at a larger radius r_{NL}) where the disturbance has definitely steepened into a nonlinear shock. It is interesting that the CIR compression and rarefaction do not form together at the same point, but this is understandable, since the latter can be considered an effect or response of the former.

To estimate which wind structures should yield the most prominent signatures in observed line profile variations, let us examine the radial Sobolev optical depth,

$$\tau_r(r,\phi) \equiv \frac{\kappa_L \, \rho(r,\phi) \, v_{\rm th}}{|\partial v_r(r,\phi)/\partial r|} \quad . \tag{6.12}$$

The gray-scale plot in Figure 6.3d shows the changes in the optical depth relative to the mean, unperturbed wind. Since both the line absorption coefficient κ_L and the ion thermal speed $v_{\rm th}$ are assumed to have the same constant values in both the mean and perturbed flow, all variations here stem from changes in the ratio of density to velocity gradient. Somewhat surprisingly, the regions of strongest optical depth enhancement occur not within the dense CIR compression (feature III), but rather within the relatively shallow velocity gradient region after the Abbott kink (feature V).

Figure 6.6 plots the radial variation of velocity and density from selected slices of constant azimuthal angle ϕ. For this corotating steady state, the changing features in these line plots also indicate the time evolution of structure at fixed azimuths. This allows us to follow the outward propagation of both the CIR density enhancement (local minima in velocity) and the trailing radiative-acoustic kink (local maxima in velocity). In the high-density CIR, the wind is either strongly accelerating or decelerating, so both the numerator and the denominator in the Sobolev optical depth (eq. [6.12]) are enhanced, resulting in very little net increase. Just outward from the kink, however, the density is nearly unperturbed, while the velocity gradient is much shallower, implying a large increase in the Sobolev optical depth. In synthetic line profiles (see Section 6.3.2 and Figure 6.13), this near plateau produces a distinct absorption feature quite similar to slowly evolving DACs. As the (corotating) steady-state structure rotates in front of the observer's line of sight, material flowing *through* the kink appears at the velocities of the local maxima in Figure 6.6, but the evolution of the feature is governed by the radiative-acoustic mode propagation, which leads to an apparent acceleration that is much slower than the actual acceleration of the wind material.

Ahead of the CIR, between the compressive density maximum and the rarefied minimum, there is a region of high acceleration that arises from the prograde

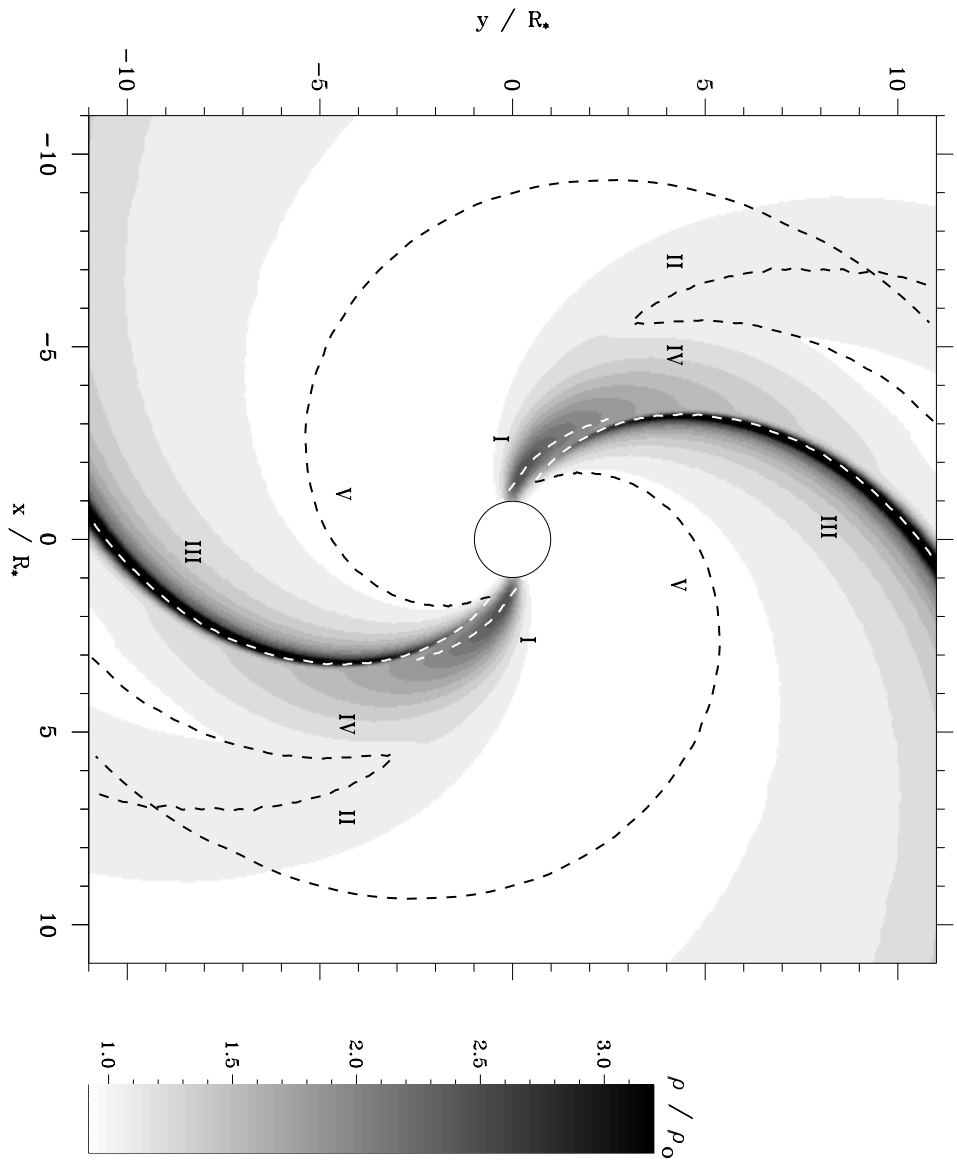

Figure 6.5: Normalized density gray-scale for Model 1, as in Figure 6.3a. Overplotted are dashed lines which trace the: (I) direct spot enhancement, (II) prograde precursor, (III) CIR compression, (IV) CIR rarefaction, and (V) radiative-acoustic Abbott kink.

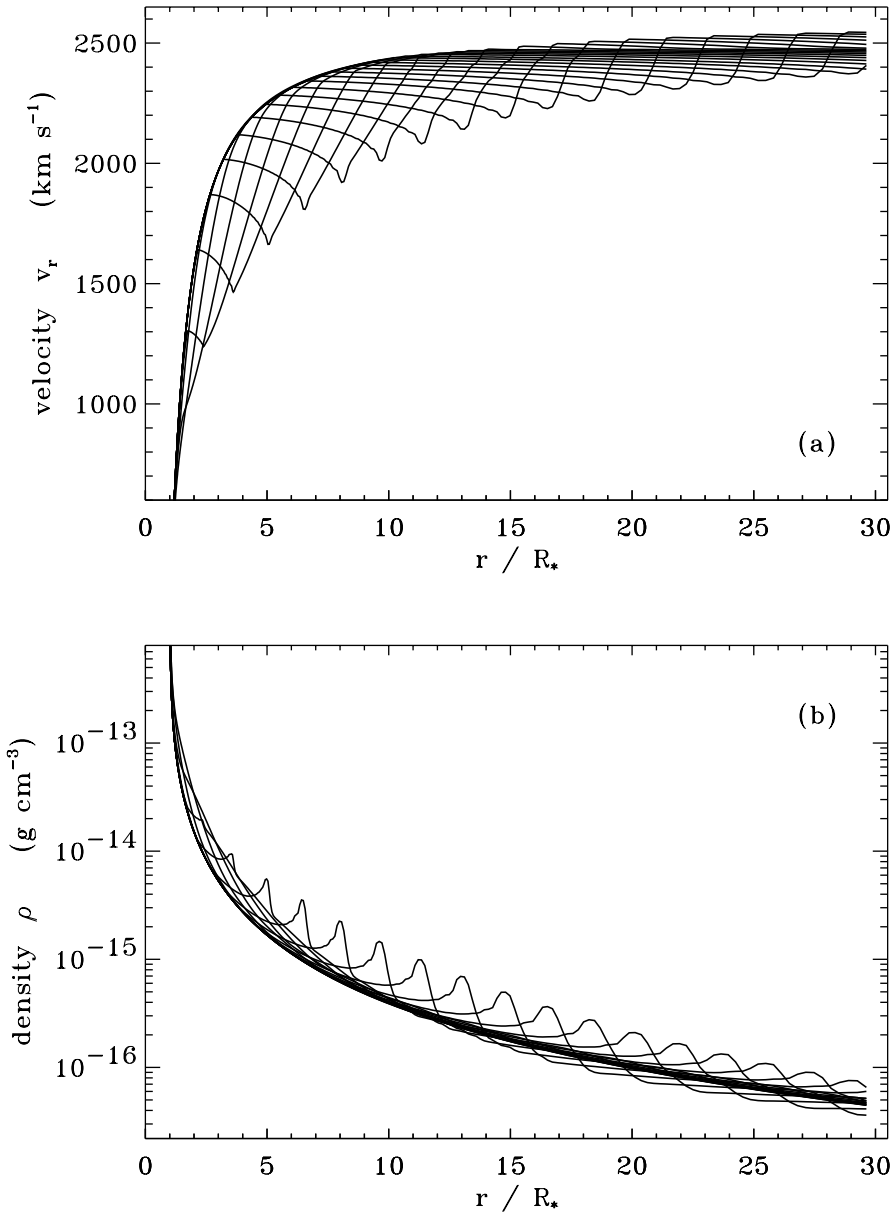

Figure 6.6: Line plots for Model 1 of the radial variation of (a) radial velocity and (b) density in the equatorial plane at 16 equally-spaced azimuthal angles, 11.25 degrees apart.

edge ($\psi > \psi_0$) of the Gaussian spot, which steepens into a monotonic sawtooth structure connecting the shock with the lower-density unperturbed wind. This region contains a lower net optical depth than the unperturbed wind, implying a relative *lack* of absorption in synthetic line profiles. This effect is only slightly weaker than the enhanced absorption due to the plateau, suggesting that isolated patches of extra absorption (DACs) may be difficult to model theoretically without a corresponding lower optical depth feature (with apparent relative "emission").

6.2.2 Standard Dark Spot: Model 2

A wind perturbed by a locally decreased radiative force ($A = -0.5$) produces a lower-density, high-speed stream, and thus settles to a steady state on the computational grid faster than a model with slow streams. Figure 6.7 shows gray-scale plots for the density, radial velocity, azimuthal velocity, and radial Sobolev optical depth for Model 2, normalized in the same way as in Figure 6.3. Although the dark spot produces an extremely rarefied wind, a high-density CIR forms (on the leading edge of the perturbation) where the high velocity stream collides with the slower unperturbed wind. The corotating structure present in Model 2 is qualitatively simpler than that in Model 1. The CIR/kink pair of features initially appears at $r_L \approx 2.2R_*$, and advects smoothly throughout the wind. There is no analog to the second pair of features (starting further out at r_{NL}) in this model.

For slices of constant ϕ, Figure 6.8 plots the radial dependence of the velocity and density. The contrast with the slow structure in Figure 6.6 is apparent. Note that the back-propagating radiative-acoustic kink is also present in this model, comprising the left edge of the flat-topped velocity peaks. However, since the kink here is a reaction to the forward-steepened shock, it forms within the fast and rarefied upstream region, and thus does not contribute strongly to the Sobolev optical depth of the corotating feature. The high density CIR also does not have an enhanced opacity because of the steep velocity gradients near the shock, as in Model 1. Indeed, Figure 6.7d shows that most of the highest optical depth material comes from the unperturbed wind, and that the high-speed CIR should be mainly a source of *decreased* absorption. The isolated "clumps" of highest optical depth in Figure 6.7d (and in Figure 6.3d) are artifacts of the finite differencing used to compute the radial velocity gradient, and do not significantly affect the volume-integrated quantities used in constructing line profile diagnostics.

The CIR structure in Model 2 appears very similar to that seen in hydrodynamic models of the solar wind, e.g., note the resemblance between Figure 6.8 and Figures 2 and 3 of Hundhausen (1973). The two major differences between solar

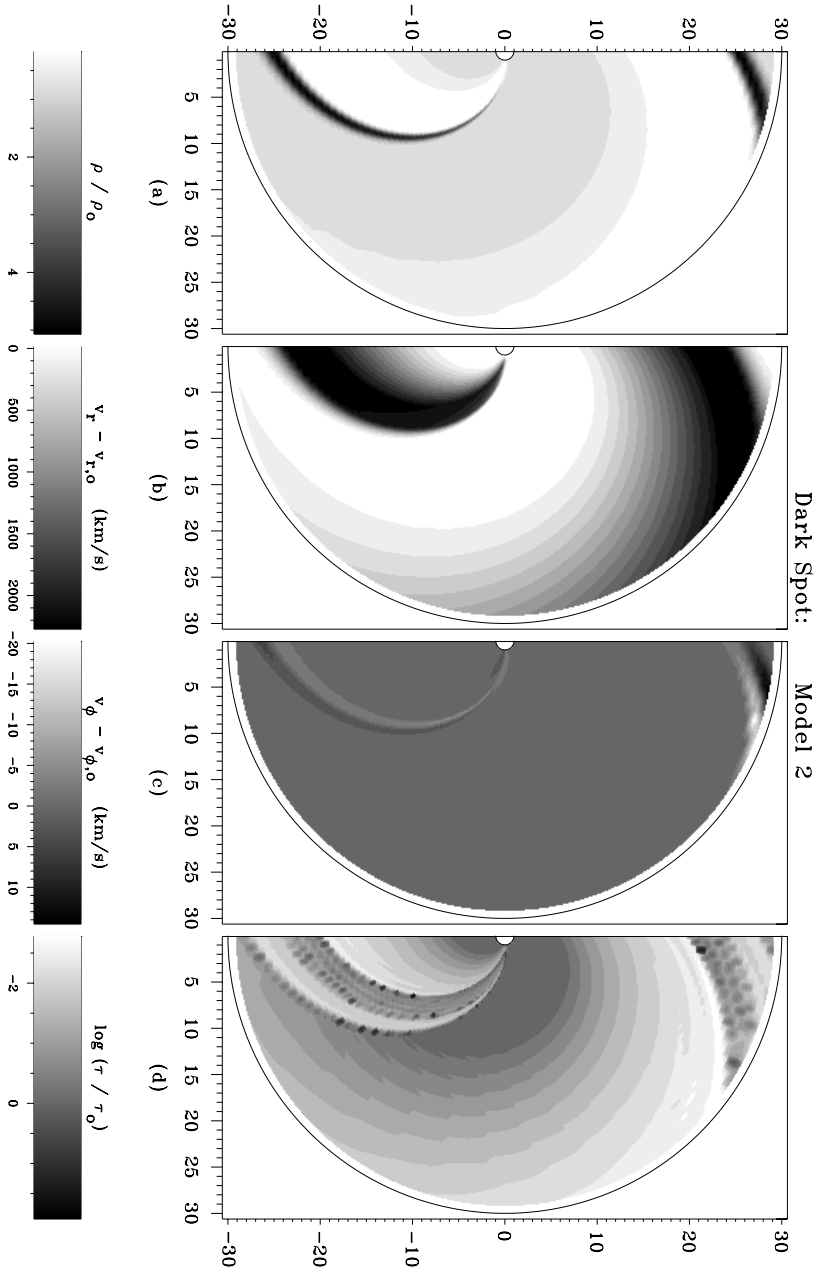

Figure 6.7: As in Figure 6.3, except for Model 2.

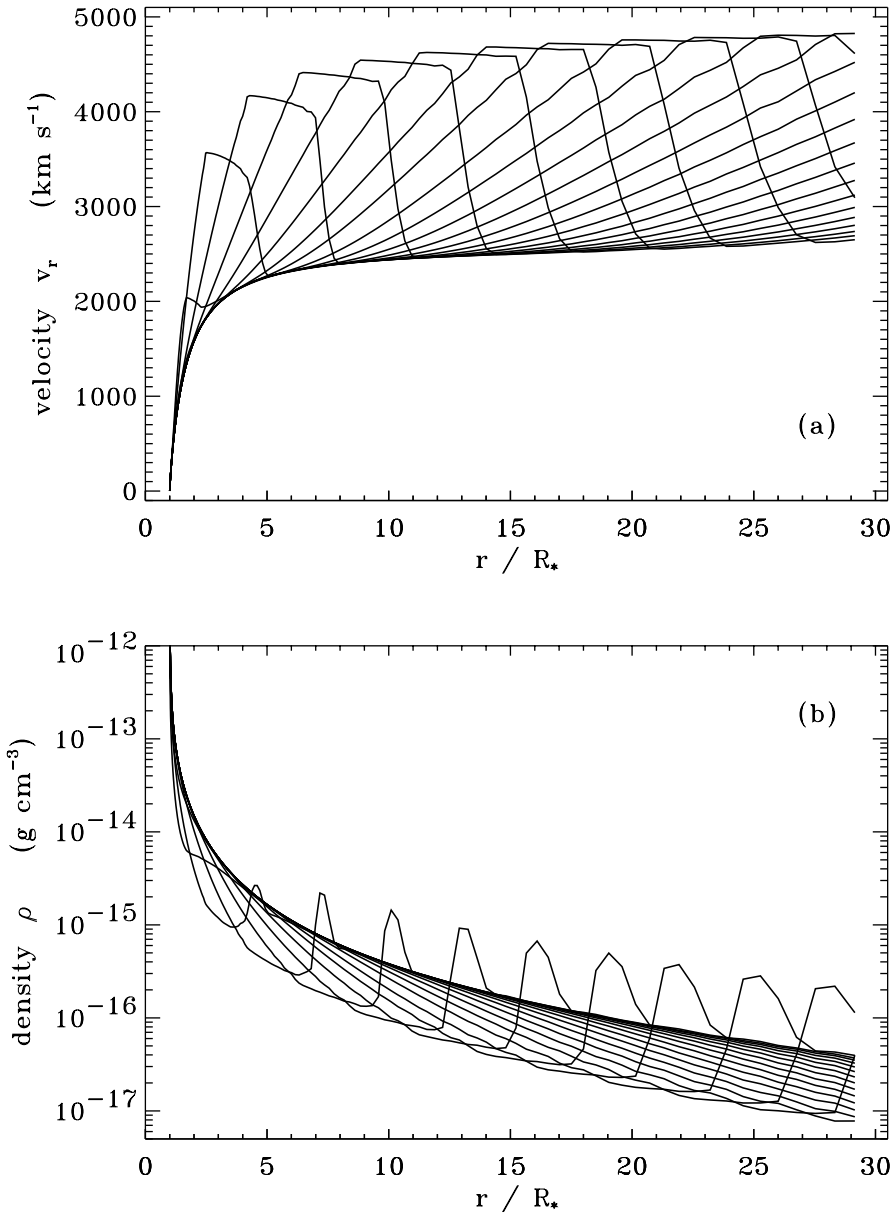

Figure 6.8: As in Figure 6.6, except for Model 2.

wind high-speed streams and those in our model are: (1) the distinct forward and reverse adiabatic shocks in the former and (2) the back-propagating radiative-acoustic kink in the latter. Despite this similarity, all subsequent models in our parameter study use the bright spot of Model 1, which promises to simulate better the slow DACs in early-type stellar winds.

6.2.3 Variation of Spot Amplitude, Width, and Stellar Rotation Velocity

Let us now examine the effect of changing various spot and wind parameters. To provide a basis for understanding the full hydrodynamical calculations, we can estimate the expected effects in terms of a simple wind streakline picture (see Figure 6.4). Note that the shape of these streaklines can be well approximated by neglecting both the wind's acceleration and the angular-momentum-conserving azimuthal velocity, which nearly "cancel each other out" when computing streakline deflection. Thus, the angular deflection is given in this approximation by the Archimedean spiral relation,

$$\phi - \phi_0 \approx -\frac{\Omega}{v_\infty}(r - r_0) \quad . \tag{6.13}$$

Mullan (1984a) used this to estimate the interaction radius r_i between a fast and slow stream initially set apart on the stellar surface by a given azimuthal separation $\Delta\phi$,

$$\frac{r_i}{R_*} = 1 + \frac{\Delta\phi}{V_{\rm eq}}\left(\frac{v_\infty^{(f)} v_\infty^{(s)}}{v_\infty^{(f)} - v_\infty^{(s)}}\right) \quad . \tag{6.14}$$

Here $v_\infty^{(f)}$ and $v_\infty^{(s)}$ are the terminal velocities of the fast and slow streams. Table 6.1 contains this simple prediction for r_i for all the hydrodynamical models in our parameter study. We assume $\Delta\phi = \Phi$, and for bright-spot models, we take the fast stream to be the unperturbed wind, and the slow stream to have $v_\infty^{(s)}$ given by equation (6.9). Conversely, for the dark-spot model the fast stream is given by equation (6.9) and the slow stream is unperturbed wind.

Models 3A, 3B, and 3C vary the spot amplitude A, and thus the direct enhancement in density and velocity over the spot (see Table 6.1). The resulting structure looks qualitatively similar to that of Model 1, but the fast/slow stream interaction takes place at different radii. Figure 6.9 traces the corresponding CIR compression and radiative-acoustic kink features for these models. As expected, CIRs form further out when there is a smaller discrepancy between the fast and slow stream speeds, but the linear minima and maxima in velocity first appear (at r_L) much closer to the star than the simple interaction analysis above predicts. The "nonlinear" radius r_{NL}, where the CIR rarefaction branches off from the prograde

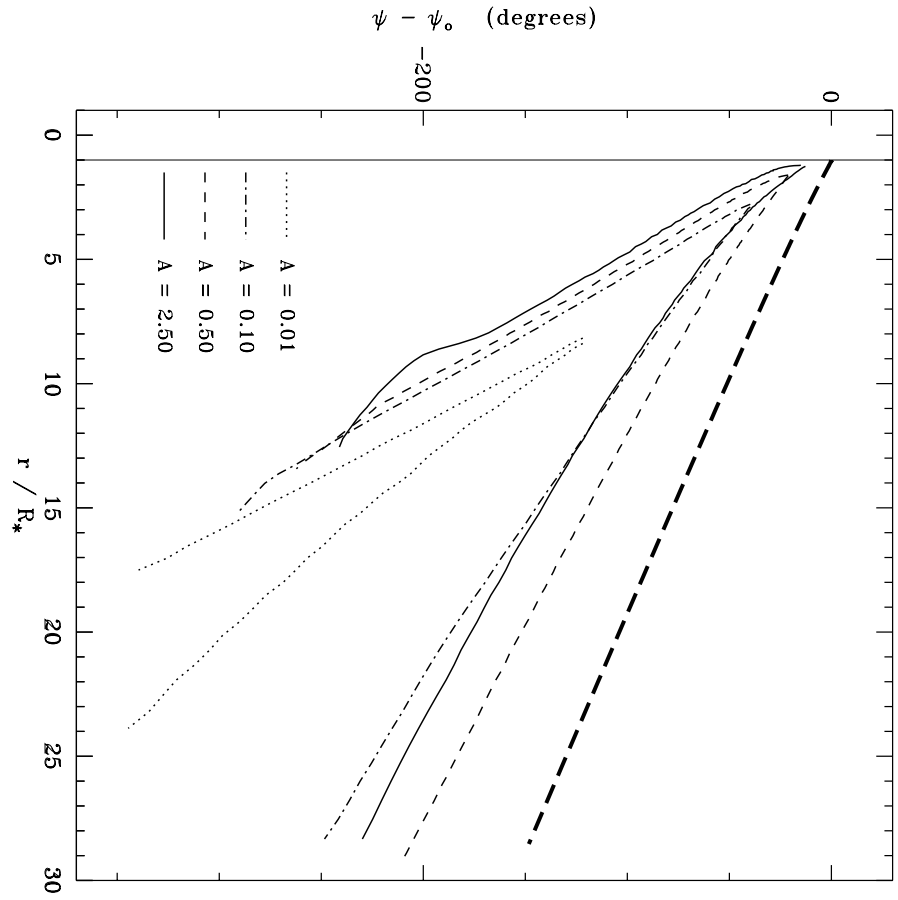

Figure 6.9: Velocity minima and maxima corresponding to CIR compression and radiative-acoustic kink features, shown for Model 1 and variable amplitude Models 3A, 3B, 3C. The heavy dashed line is the streakline for the unperturbed one-dimensional standard model wind.

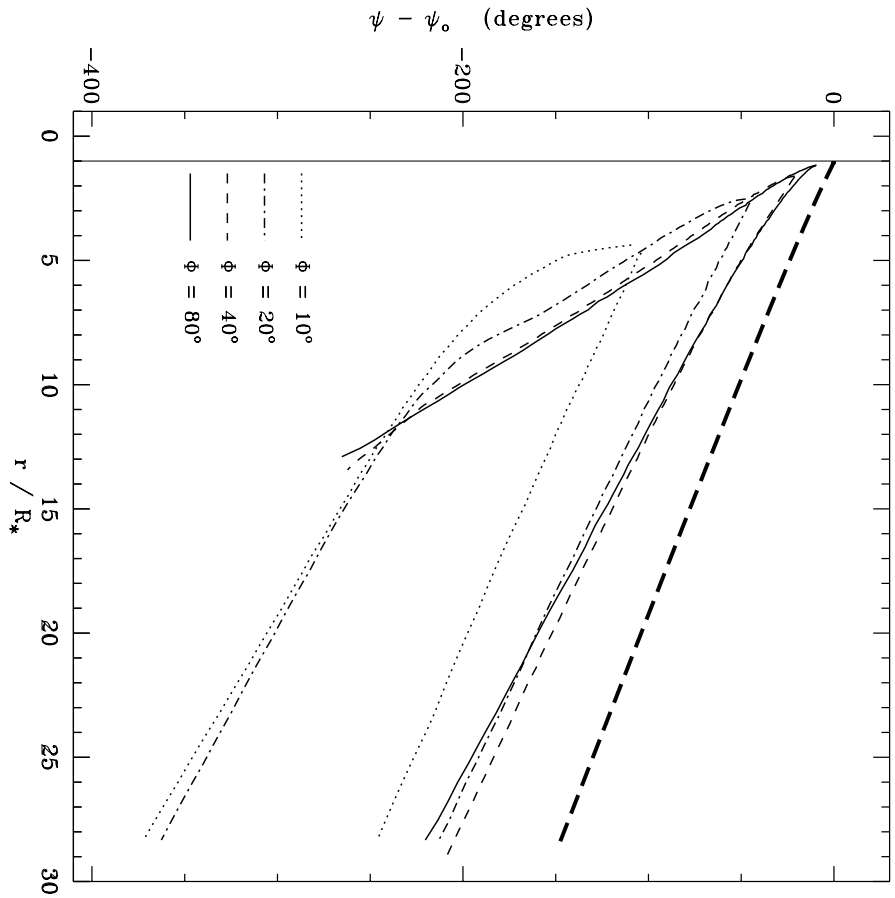

Figure 6.10: As in Figure 6.9, except for Model 1 and variable spot-width Models 4A, 4B, 4C.

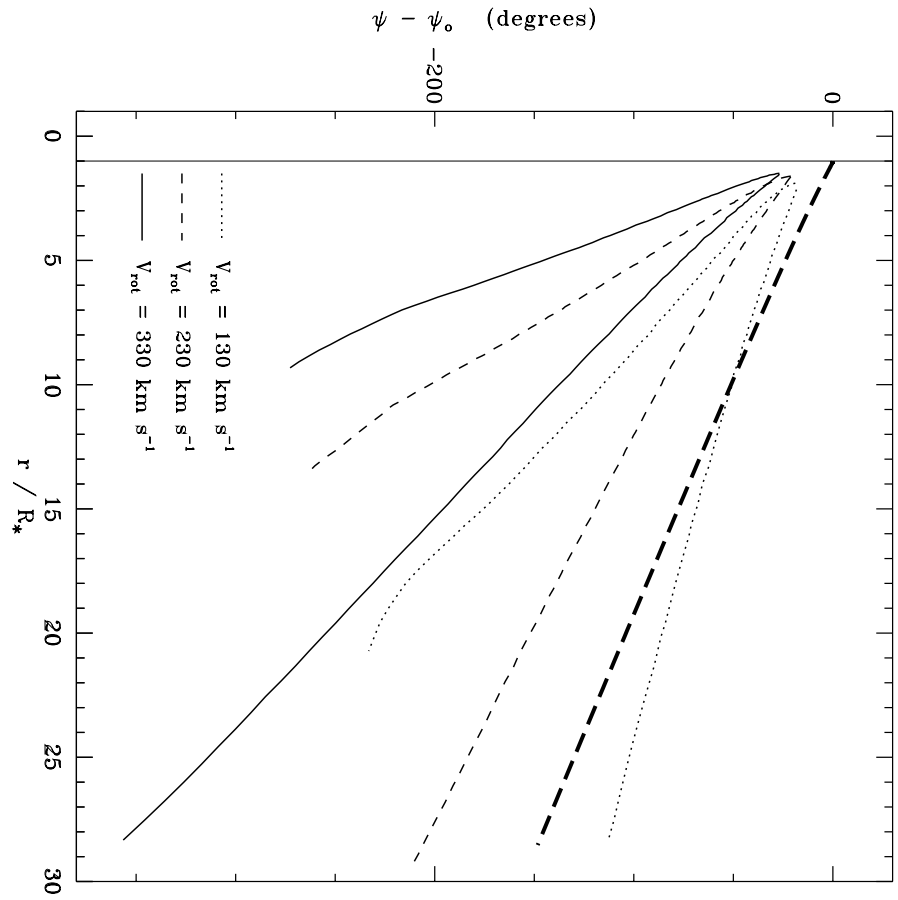

Figure 6.11: As in Figure 6.9, except for Model 1 and variable rotation Models 5A, 5B.

dense precursor, is relatively *constant* with A, indicating a qualitatively different formation mechanism from the compression/kink features.

Figure 6.12 shows how the velocity law of the kink and CIR shock varies with spot amplitude, with each model rotated in azimuth to line up similar features. For the smallest values of A (0.01, 0.1), no shock has yet formed, so both features appear "kink-like," propagating nearer to the slow radiative-acoustic mode speed than to the mean wind speed (see Figure 6.9). The shock steepening is evident for larger values of A, and the most extreme model ($A = 2.50$) shows considerable slowing of the dense CIR resulting from the inverse dependence of the radiative force with density (e.g., eq. [2.88]). Our canonical Model 1 CIR, then, seems just on the verge between both "slowing" mechanisms, as well as having a shape between the low-A weak discontinuities and the high-A shocks. In all cases, however, the decelerating plateau-region ahead of the kink has the same characteristic (negative) acceleration, indicating that the enhanced optical depth at this radius may not vary strongly with spot amplitude.

Models 4A, 4B, and 4C vary the azimuthal spot width Φ, and Figure 6.10 shows their CIR compression and kink features. Increasing or decreasing the full-width Φ simply alters the spatial scale of the interactions, and, in the limit of very small spots (where the star's sphericity can be neglected) the CIR structures seem self-similar with respect to an overall expansion factor. Table 6.1 indicates an inverse relationship between Φ and the maximum CIR density, and this can be understood heuristically by the fact that when a given spot amplitude is spread over a larger area, the collision of fast and slow streams is more diluted, and the resulting shocks are not as strong. Model 4A, with the smallest width $\Phi = 10°$, shows an apparent reversal in this trend, and we suspect that some of the detailed shock structure is under-sampled in our relatively coarse (in this case) azimuthal grid. Note that Mullan's (1984a) interaction radius r_i agrees well with the location of the nonlinear rarefaction/precursor feature r_{NL} for these models.

Observations (Prinja 1988; Henrichs et al. 1988) suggest that the recurrence and acceleration times of DACs tend to vary inversely with the projected equatorial rotation speed, $V_{\rm eq} \sin i$. To examine how well our dynamical models might reproduce these observed trends, Models 5A and 5B vary the equatorial stellar rotation velocity $V_{\rm eq}$. Figure 6.11 shows their CIR compression and kink features. The dominant effects are the overall variation of the spiral streaklines (see, e.g., eq. [6.13]), and the inverse centrifugal dependence of v_∞ on the rotation rate (Friend & Abbott 1986). The strength of the CIR shock decreases for more slowly rotating stars, and we believe that this results from the variation of the streaklines with respect to the star-spot enhancement (Figure 6.1). Perturbed gas which rapidly advects out of the region of direct enhancement receives less of a "boost" of extra density, and thus

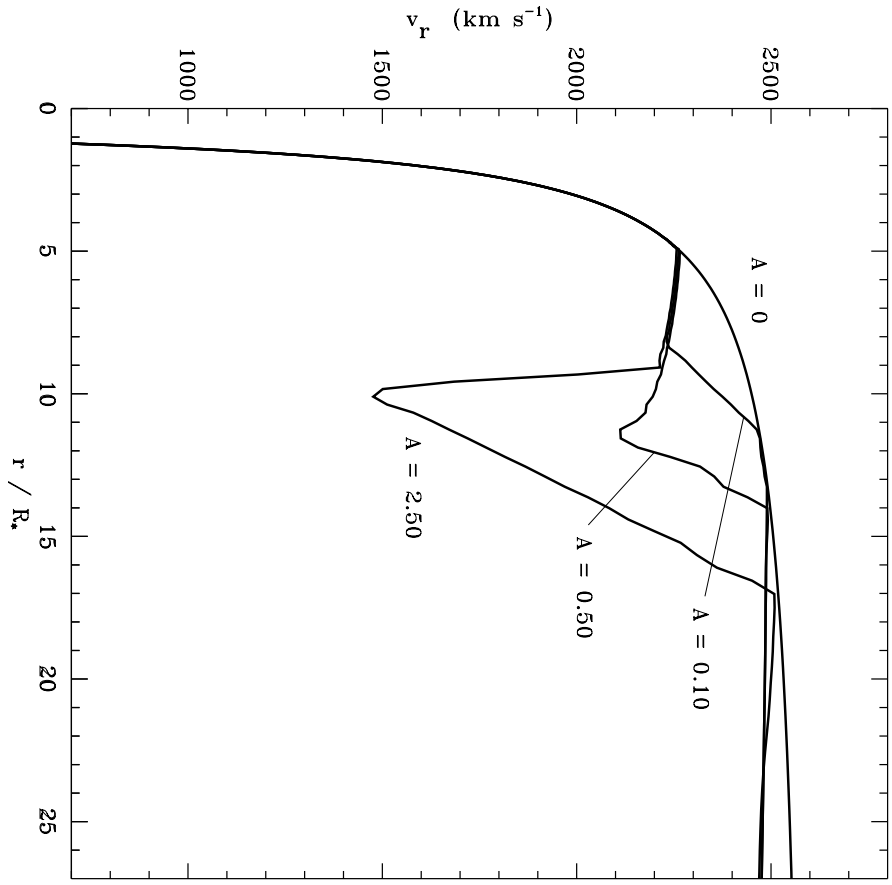

Figure 6.12: Radial velocity showing the radiative-acoustic kink and CIR shock for models with varying spot amplitude. Each ϕ slice was chosen independently to align the initial kink deceleration at the same radius.

does not form as strong a compression when interacting with the ambient wind.

6.3 Synthetic Observational Diagnostics

6.3.1 SEI Line Profile Construction

Ultraviolet P Cygni lines are sensitive probes of the wind structure of hot luminous stars, and it is important to model accurately observed variations in their profile shape. Here we use a multidimensional extension of the SEI (Sobolev with Exact Integration) method of Lamers, Cerruti-Sola, & Perinotto (1987), discussed in Chapter 3, to compute synthetic line profiles. In this method, the source function is calculated locally in the wind using the Sobolev escape probability approximation, and the emergent flux profile is computed by numerically integrating the formal solution to the transfer equation. Bjorkman et al. (1994) discuss a two-dimensional extension of the basic SEI algorithm, and our computational approach is similar in that we do not yet treat the general case of nonlocal (or line doublet) resonance coupling. Our method, however, efficiently computes line profiles from an arbitrary three-dimensional distribution of density and velocity, for observers at arbitrary vantage points.

Following the notation of POF, we parameterize the opacity of a model pure-scattering resonance line by defining a dimensionless line-strength

$$k_L \equiv \left(\frac{\dot{M} v_{\rm th}}{4\pi R_* v_\infty^2} \right) \kappa_L \ , \tag{6.15}$$

where v_∞ and $\dot{M}$ are taken from the unperturbed model wind. We assume the mass absorption coefficient κ_L is constant in radius, which is valid for lines of interest in the dominant ionization stage of the wind, and at least allows qualitative comparison for other lines. We consider two representative cases: a moderate unsaturated line ($k_L = 1$) and a strong saturated line ($k_L = 100$).

The local two-dimensional (solid angle) integrals required to obtain the escape probability and core-penetration probability for the Sobolev source function are computed using Romberg's successive refinement algorithm. The explicit form of these integrals is found in Lamers et al. (1987). POF compare the use of the local Sobolev formalism with a self-consistent multiple-resonance technique in structured wind models, and find significant disagreement in the resulting line profiles. However, our CIR model winds are much less structured than the one-dimensional instability models used by POF, with at most only two zones of nonmonotonic velocity variation in the entire wind. Further, here we concentrate on *residual* line profile variability, which should be less susceptible to consistency errors in the source function than the actual line profile shape.

We perform the "exact integration" for the line flux using a cylindrical (p', ϕ', z') coordinate system with the observer oriented along the positive z'-axis at an infinite distance from the origin. The equation of radiative transfer is evaluated in differential form along rays parallel to this axis, and along each ray the specific intensity is integrated using second order implicit Euler differencing. The resulting emergent intensities at the outer boundary of the computational grid are then integrated by nested Romberg quadrature in p' and ϕ' to form the flux, and this process is repeated for each frequency point in the total line profile. We refer the reader to Lamers et al. (1987) and POF, who summarize these integrals, but only apply them in the spherically symmetric (ϕ' independent) case.

We make two major approximations in our line profile construction technique:

1. The three-dimensional wind structure is formed by interpolating in latitude between the two-dimensional equatorial plane models and the one-dimensional unperturbed polar wind. For simplicity we assume the same Gaussian structure of the "star spots" in latitude as in longitude, and apply it to the entire wind:

$$\begin{aligned} \rho(r,\theta,\phi) &= \rho^{(0)}(r)\,[1 - E(\theta)] + \rho^{(2\mathrm{D})}(r,\phi)\,E(\theta) \\ v_r(r,\theta,\phi) &= v_r^{(0)}(r)\,[1 - E(\theta)] + v_r^{(2\mathrm{D})}(r,\phi)\,E(\theta) \\ v_\phi(r,\theta,\phi) &= v_\phi^{(0)}(r)\,[1 - E(\theta)]\,\sin\theta + v_r^{(2\mathrm{D})}(r,\phi)\,E(\theta)\,\sin\theta \quad , \end{aligned} \tag{6.16}$$

   where $E(\theta) \equiv \exp[-(\pi/2 - \theta)^2/\sigma^2]$ (see eq. [6.2]). As in the two-dimensional models, we retain our assumption that $v_\theta = 0$. Note that the azimuthal velocity has an extra factor of $\sin\theta$ included to preserve angular momentum conservation out of the equatorial plane, and this provides a latitudinal wind variation even for *unperturbed* models.

2. The total Doppler width of the Gaussian line profile contains both thermal and microturbulent contributions,

$$v_D \equiv \sqrt{v_{\mathrm{th}}^2 + v_{\mathrm{turb}}^2} \quad , \tag{6.17}$$

   with the thermal speed set by $v_{\mathrm{th}} = 0.28a$, as appropriate for CNO driving ions. For simplicity, we assume a constant microturbulent velocity $v_{\mathrm{turb}} = 100\,\mathrm{km\ s^{-1}}$, though better line-profile fits have been obtained by assuming this varies in proportion to the mean wind velocity (Haser et al. 1995). Though phenomenological, this use of a microturbulent velocity allows realistic line-profile synthesis with a minimum of free parameters. It also compensates for the suppression here of the small-scale instability, which one-dimensional, nonlocal simulations have shown to result in many of the same observational signatures as microturbulence (POF; Owocki 1994).

6.3.2 Time Variability in Dynamical Models

We produce time-variable P Cygni line spectra by positioning an "observer" in the equatorial plane ($i = 90°$) at successive azimuthal angles ϕ with respect to the two-dimensional models. For the standard rotation velocity used in Models 1, 2, 3, and 4, the line profile variability repeats with a period

$$\Pi = \frac{\pi R_*}{V_{\rm eq}} = 2.091\,{\rm days} \quad . \tag{6.18}$$

Of course, since spiral streakline structures in the models often subtend more then 180° of azimuth, continuous DAC-like signatures can exist for times longer than this period. We arbitrarily define $t = 0$ when the observer is positioned directly over the center of one of the photospheric spot perturbations.

As emphasized by Lamers (1994), we find that most of the line profile variability occurs in the absorption column of the wind ($0 \leq p' \leq R_*$), with comparatively little variation in the larger emission volume ($p' > R_*$). Because the flux integration over this emission volume dominates the CPU time in our SEI line-profile synthesis, we only computed full, variable emission-volume profiles for a few selected test cases, namely for observers at four equally-spaced azimuthal angles ($\phi = 0°, 45°, 90°, 135°$) for Model 1, as well as at one arbitrary azimuthal angle for an unperturbed ϕ-independent wind model. For an unsaturated ($k_L = 1$) line, we found that the perturbations in the absorption-column flux reach as high as 47% of the continuum level, whereas those in emission-volume flux never exceed 1.9%. Since these latter variations would only be marginally observable with IUE signal-to-noise ratios of 20 to 40, we neglect the perturbed emission volume when computing subsequent line profiles on a finer time- and velocity-sampled grid.

Figures 6.13 and 6.14 show the absorption-column line profile variability for Model 1, repeated over three data periods (1.5 rotation periods) to emphasize the rotationally-modulated structure. Following the standard observational convention, the gray-scale is normalized by a "minimum absorption" (maximum flux) template, constructed independently at each line velocity. This choice contains the implicit bias that the variability takes the form of extra *absorption,* which is only partly appropriate for Model 1. The unsaturated ($k_L = 1$) line exhibits definite DACs that apparently accelerate through the profile on ~3.9-day time scales, even though their recurrence time is shorter. The saturated ($k_L = 100$) line exhibits blue-edge variability on the same time scale (see below). Figures 6.13 and 6.14 also contain the time-averaged line profiles for Model 1 and the minimum and maximum absorption templates, which show the extent of the absorption variability at each velocity. We also plot the standard deviation of the data, allowing a qualitative comparison to observed temporal variance spectra.

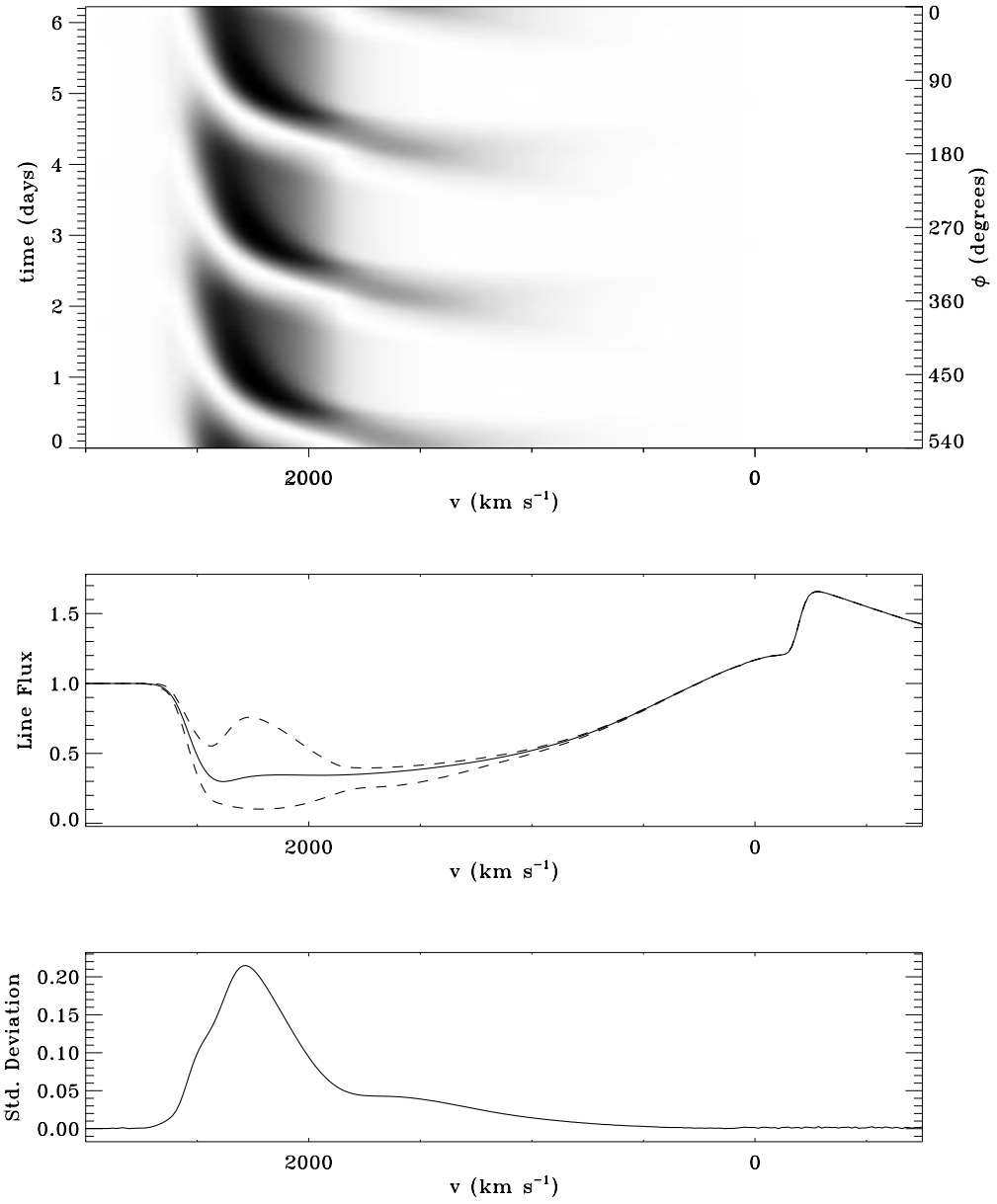

Figure 6.13: SEI absorption-column line variability for Model 1, computed for an unsaturated line. The gray-scale values range from white (maximum flux) to black (minimum flux), measured relative to the dashed-line templates in the middle panel. The solid lines show the time-averaged line profile, in the middle panel, and the standard deviation, or square root of the variance, in the bottom panel.

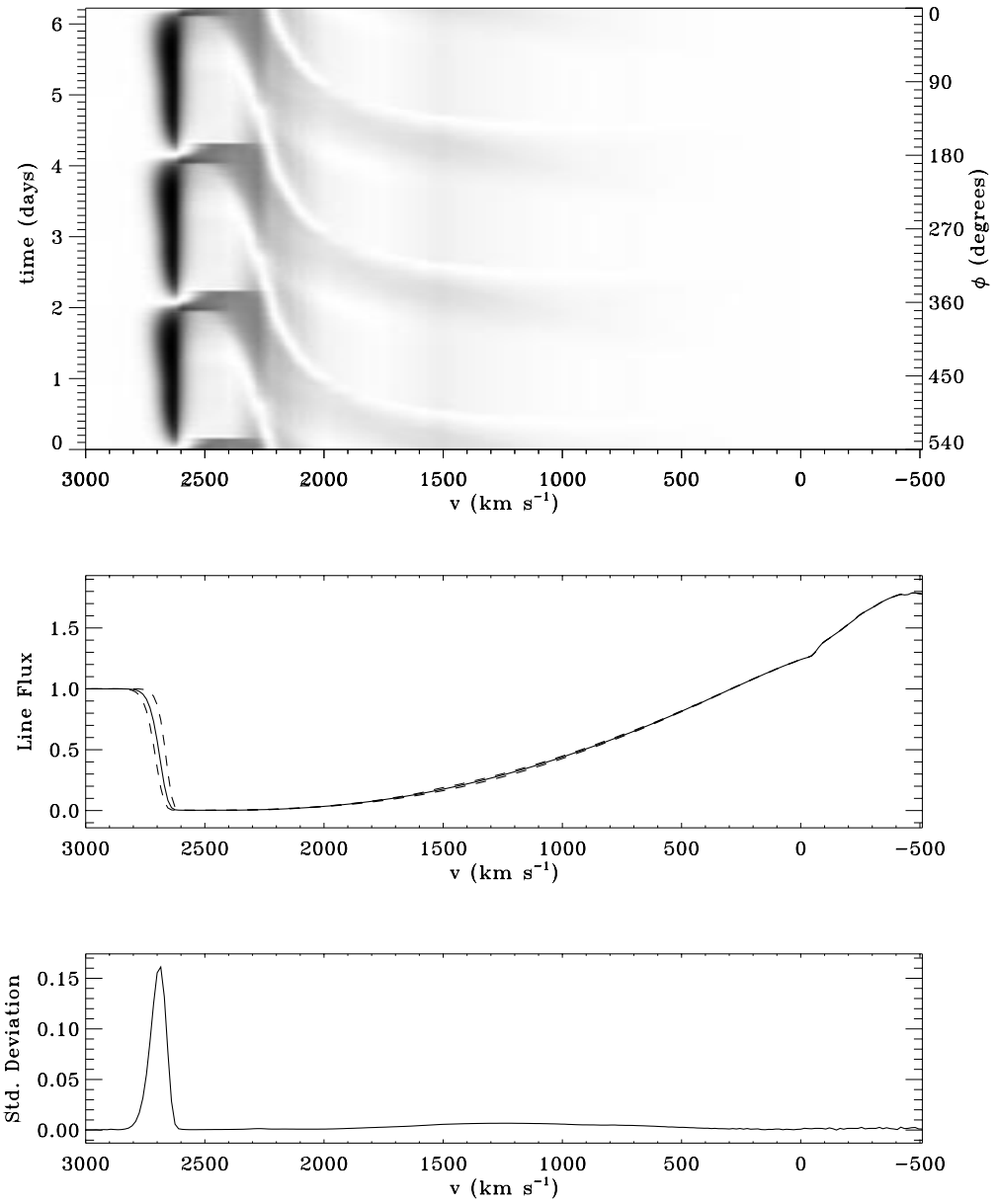

Figure 6.14: As in Figure 6.13, except for a strong saturated line. The gray-scale variability between 1000 and 2550 km/s is deceiving (there is actually *negligible* variability) because of the observational convention of *dividing* by the minimum absorption flux, which here approaches zero.

Figure 6.15 shows the absorption-column line profile variability for Model 2. The accelerating features in this unsaturated ($k_L = 1$) line differ from those in Figure 6.13 in two apparent ways. First, because of the high-velocity stream induced by the dark spot, the variability extends out to nearly 5000 km s^{-1}, almost twice the unperturbed wind terminal speed. Second, the enhanced absorption at lower line velocities ($v \lesssim 2000\,\mathrm{km\ s^{-1}}$) represents the mean state, and the isolated accelerating features appear as a lack of absorption. Although we anticipated this trend in Section 6.2.2, it is surprising to note the overall *similarity* between the bright and dark spot profiles at higher line velocities ($2000\,\mathrm{km\ s^{-1}} \lesssim v \lesssim 2400\,\mathrm{km\ s^{-1}}$). The primary difference here is that the strongest absorption feature trails, in Model 1, and leads, in Model 2, the overall region of enhanced absorption. Far from the star, the near-terminal-speed wind is beginning to laterally homogenize the bright or dark spot perturbations into a simpler pattern of alternating large-scale compressions and rarefactions.

The extreme blue edges of saturated ultraviolet wind lines from hot stars are observed to fluctuate in position and strength (Prinja et al. 1992; Henrichs et al. 1994; Kaper 1993, Chapter 6; Kaper et al. 1996), indicating that variable amounts of rarefied gas exist at velocities in excess of the terminal velocity. In dynamical models of structure in line-driven winds, such high speed rarefactions arise quite naturally from the tendency of the line acceleration to scale inversely with the flow density. One extreme example is the very rarefied, high-speed flows that form from the small-scale instability intrinsic to the line-driving (see, e.g., Owocki et al. 1988; Owocki 1994; Feldmeier 1995). But this also holds for the large-scale structure arising from both the dark and bright spot models computed here. In the case of the dark spot, Model 2, the variation at high velocity is quite extreme, greater than ever observed, and this provides a strong argument against such large-scale dark spots and their associated rarefied high-speed streams in hot-star winds. For the bright-spot models, the blue-edge modulation is more moderate, and generally consistent with the observed variability.

However, observations generally indicate that the velocity of saturated absorption ("v_{black}") remains relatively constant, with most of the variation attributed to changes in the steepness of the blue-edge rise to the continuum (Prinja et al. 1992; also Kaper 1993); in contrast, in the model here, the black velocity exhibits nearly the same variation as the overall edge. This model further predicts a quite distinctive phase correspondence between the maximum extent of the blue edge of saturated lines (Figure 6.14) and the blueward asymptotic extension of DACs in unsaturated lines (Figure 6.13). This seems in qualitative agreement with some of the observational trends noted by Kaper et al. (1996), though in general the relationship among the various types of line-profile variability can be quite complex (Prinja et al. 1992). In particular, the blue-edge, high-velocity variation sometimes

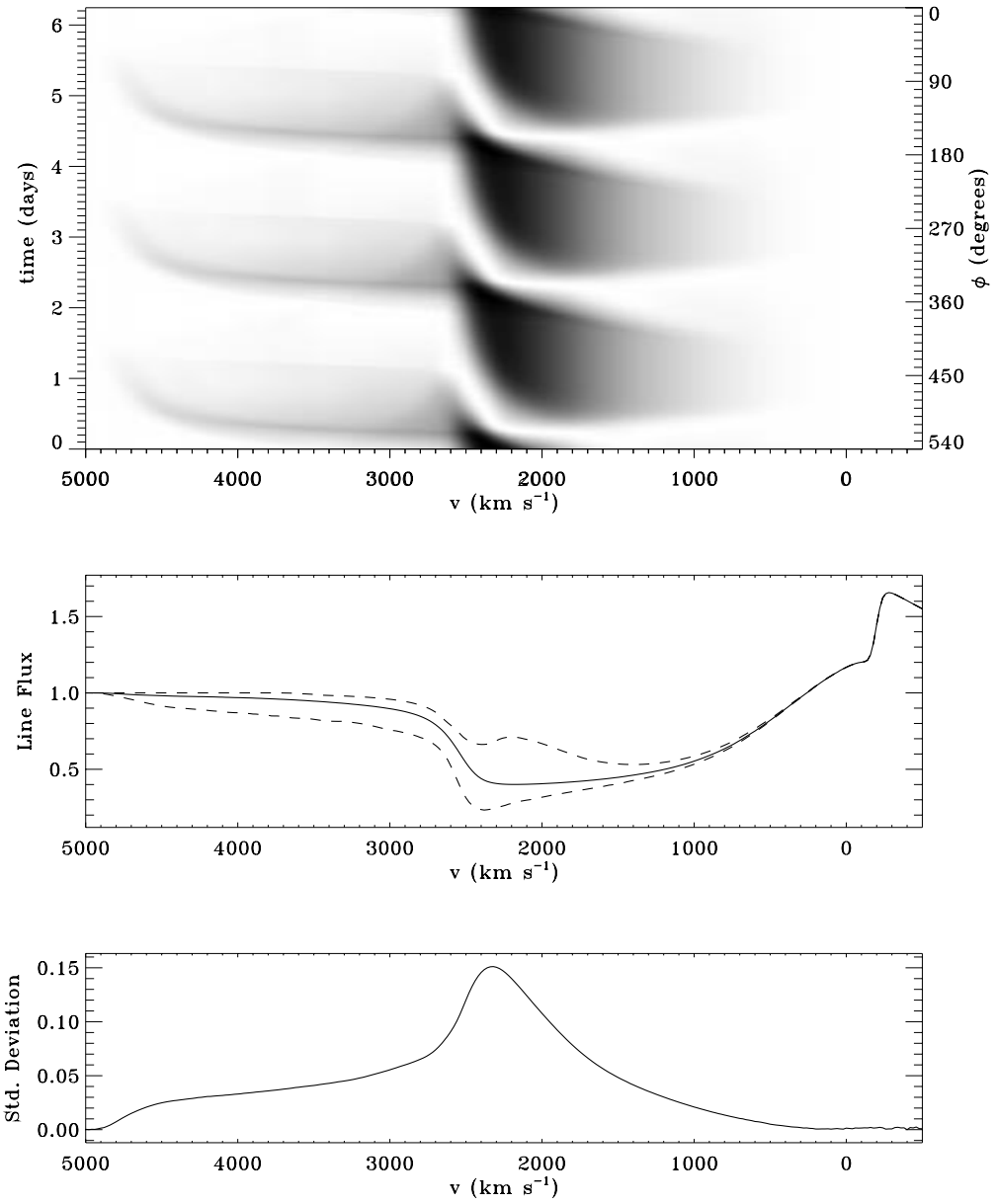

Figure 6.15: As in Figure 6.13, except for Model 2.

shows strikingly close correspondence to the behavior in *low-velocity* line diagnostics (e.g., He II λ4686, Kaper 1993, Chapter 6), and such behavior does not appear to have a clear explanation in the context of the simple CIR models presented here.

In order to interpret more clearly the evolution of DACs in our models, we utilize the observational fitting technique of Henrichs et al. (1983) and Kaper (1993), which represents the DACs as dense, plane-parallel slabs of gas in the observer's line of sight. For each component, the dependence of the quotient flux (normalized by the minimum absorption template) on the line-of-sight velocity v is fit by

$$I(v) \;=\; \exp\left\{-\tau_c \exp\left[-\left(\frac{v - v_c}{v_t}\right)^2\right]\right\} \quad , \tag{6.19}$$

where τ_c is a representative central optical depth, v_c is the line velocity of the center of the DAC, and v_t is related to its width in velocity space. These three parameters are varied and fit to each feature in the time series using Marquardt's χ^2 method (Bevington 1969). Although many of our synthetic DACs are asymmetric about v_c, with slightly more absorption on the low-velocity side of the feature, the fits always reproduce well the overall line shape. One additional useful quantity, the column density of the DAC, is given for our model lines by

$$N_{col} \;=\; \frac{\sqrt{\pi}}{\kappa_L v_{\rm th} \langle m \rangle} \frac{\tau_c v_t}{(1 + v_c/c)} \quad , \tag{6.20}$$

where $\langle m \rangle$ is the mean mass of gas atoms and ions (see POF and Kaper 1993).

In Figures 6.16, 6.17, and 6.18 we plot the resulting fit parameters (v_c, v_t, N_{col}) as a function of time for the bright-spot, unsaturated-line models in the parameter study. The inherent "overlap" in the time series (i.e., multiple DACs at a given time) has been removed to more clearly show the evolution of the individual DAC. As is often seen in observed line profile variability, the feature accelerates through the line profile while growing progressively narrower, its column density increasing to a maximum value, then decreasing as the DAC nears its terminal velocity. In our models, v_c often reaches or exceeds the wind's unperturbed v_∞, but the rapidly dropping values of N_{col} (which also is related to the equivalent width of the DAC) might preclude actual observation of this final period of evolution. In fact, most of the DACs we track seem to approach an initial "pseudo terminal speed" ($\sim$ 0.8-0.9 v_∞) while the column density is at its peak, then accelerate further to the wind's terminal speed as the column density decreases.

As expected, the DACs produced by radiative-acoustic kinks accelerate quite slowly. Figure 6.18 compares the acceleration of DACs from Models 1, 5A, and

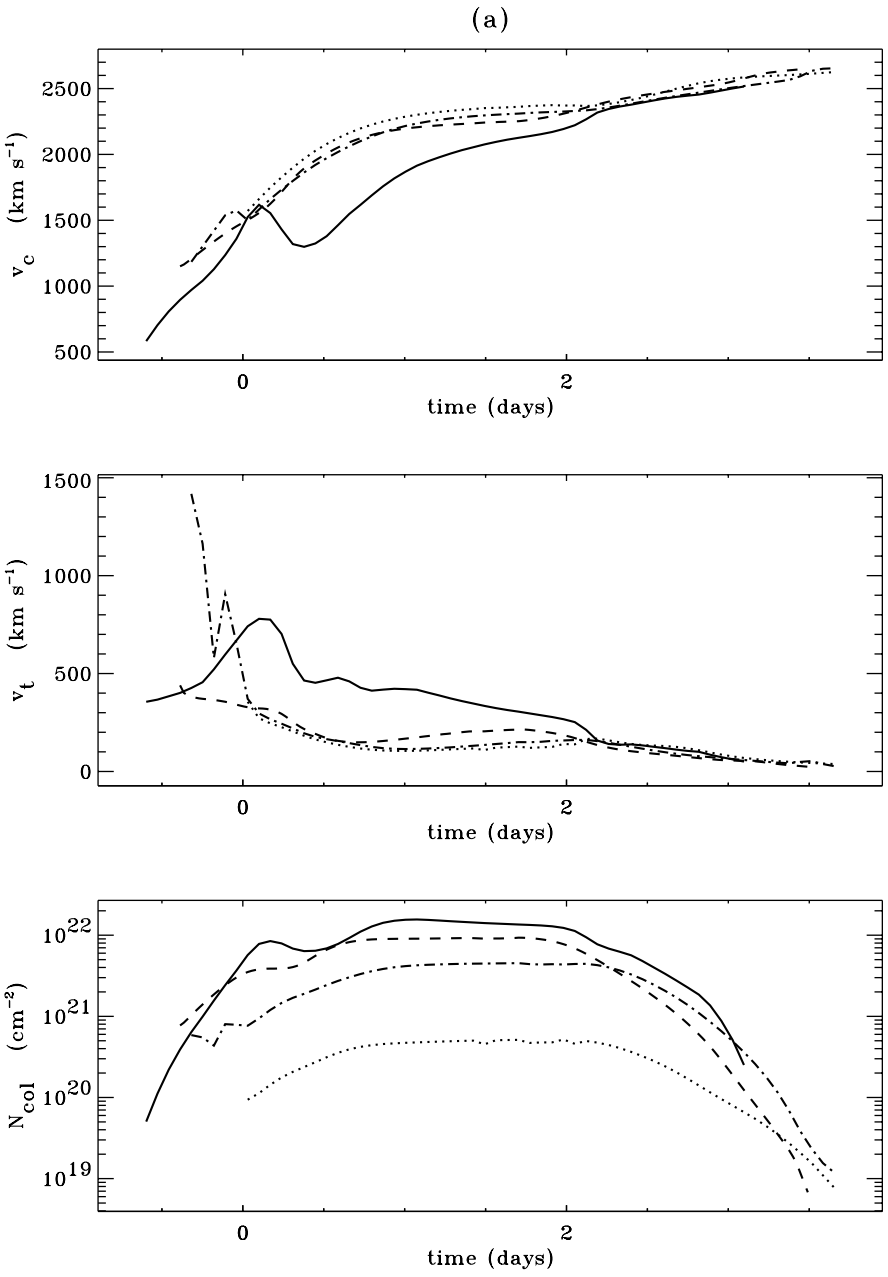

Figure 6.16: Best-fit DAC features: central line velocity, characteristic width, and slab-model column depth, shown for Model 1 and variable amplitude Models 3A, 3B, 3C. Here we plot the DAC from only a *single* stream structure, so as not to clutter the plot with multiple DACs at a given time. The line styles for each set of models are identical to those in Figure 6.9.

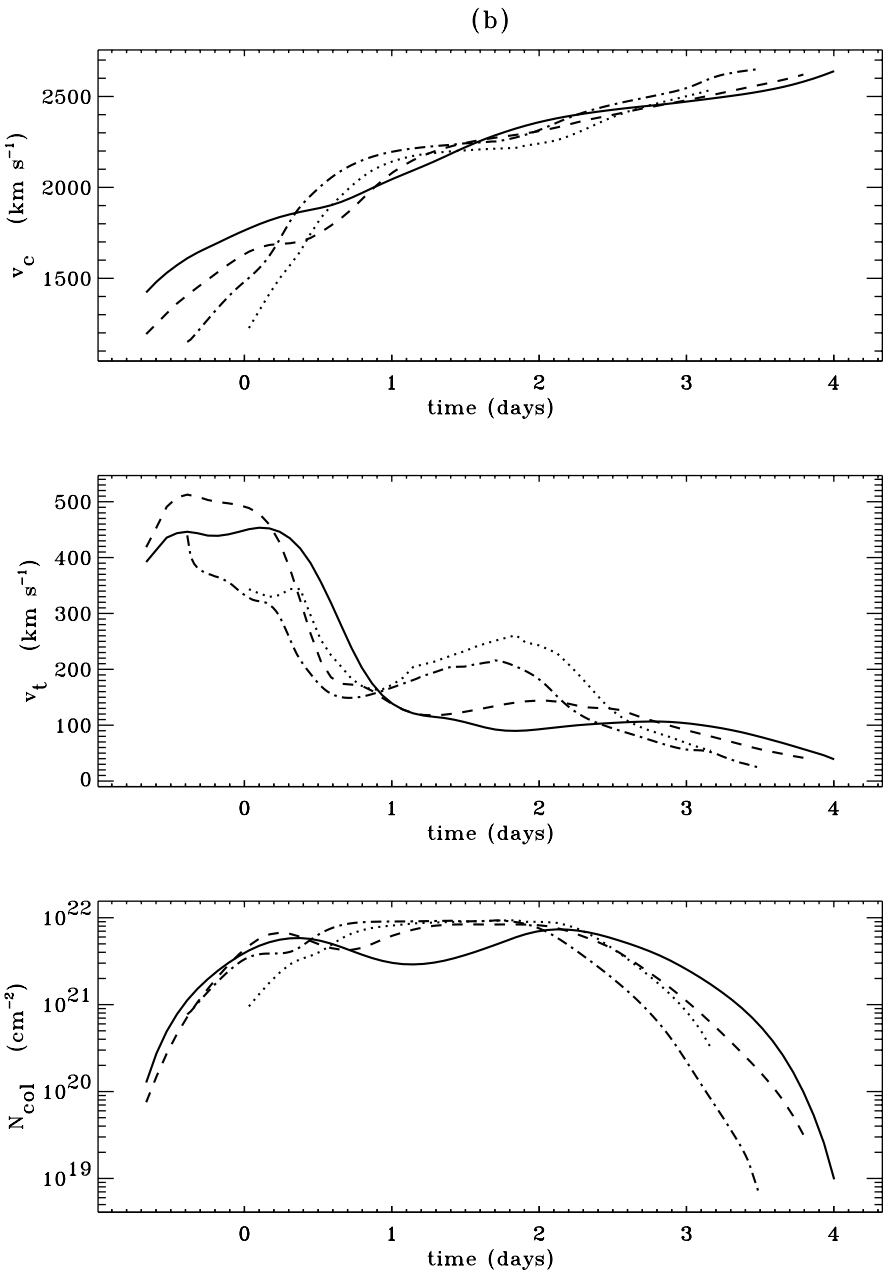

Figure 6.17: As in Figure 6.16, except for Model 1 and variable spot-width Models 4A, 4B, 4C. The line styles correspond to those in Figure 6.10.

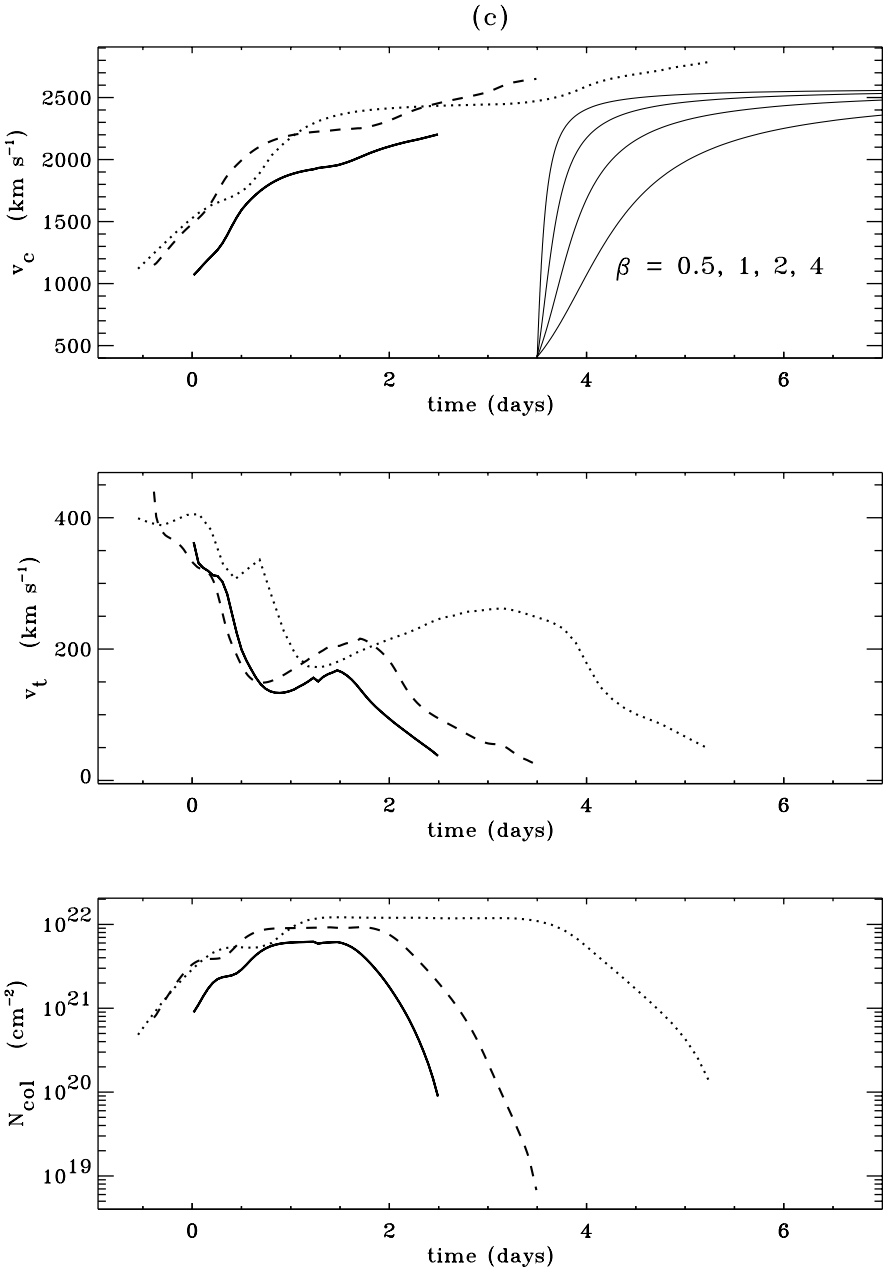

Figure 6.18: As in Figure 6.16, except for Model 1 and variable rotation Models 5A, 5B. The line styles correspond to those in Figure 6.11.

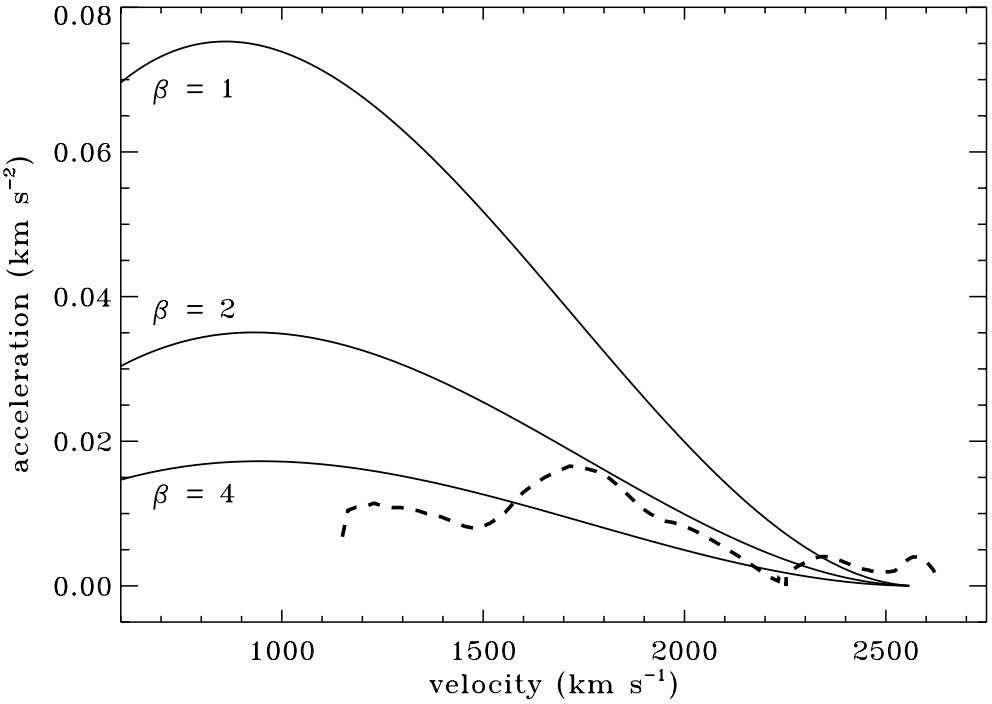

Figure 6.19: DAC acceleration versus velocity for Model 1 (dashed line) and analytic "beta" velocity laws (solid lines).

5B with several analytic "beta" velocity laws. We compute $v(t)$ by numerically integrating the kinematic relation

$$t = t(r[v]) = \int_{R_*}^{r} \frac{dr'}{v_0 + (v_\infty - v_0)(1 - R_*/r')^\beta} \ , \tag{6.21}$$

where we take $v_0 = a$ and $v_\infty = 2580\,\mathrm{km\ s^{-1}}$. The slow acceleration of the DACs is equivalent to $\beta \approx 2 - 4$, which agrees with the observations of Prinja et al. (1992) and Prinja (1994). Note, however, that an estimation of a single characteristic β for a DAC is problematic, since (1) its terminal speed is not clearly defined, and (2) $v_c(t)$ experiences several minor acceleration and deceleration episodes superimposed on the overall DAC acceleration. Figure 6.19 plots acceleration versus velocity for the DAC of Model 1, and compares it to the beta laws defined above. The small-scale irregularity at velocities greater than about $2200\,\mathrm{km\ s^{-1}}$ is likely due to numerical errors in computing the acceleration $\partial v_c/\partial t$ from velocities on a finite grid of "observation times." The nonmonotonicity in Figure 6.19 at velocities less than $2200\,\mathrm{km\ s^{-1}}$ reflect the fact that the kink structures are dynamically quite complicated, with varying line-of-sight velocity behavior at different radii and viewing angles. Thus the apparent acceleration of DACs is not fit very well with simple "beta" velocity law. Indeed, in both magnitude and nonmonotonic character, the apparent accelerations here are actually quite similar to those in actual DAC observations, e.g., those found by Prinja et al. (1992) in the wind of ζ Puppis.

6.3.3 Continuum Polarization Variations

Figure 6.20 shows optically-thin electron-scattering polarization from the standard (bright spot) Model 1, computed by integrating over the solid angle subtended by a uniformly-bright (non-spotted) spherical star. The equatorial density variations have been extended to other latitudes as described in eq. (6.16) above, and the polarization for observers at different latitudes (i.e., inclinations) and longitudes (i.e., phases) has been calculated. As in previous plots, time decreases as phase increases. For equator-on ($i = 90°$) views, all polarization is in the Q-plane, and the variation in magnitude is nearly sinusoidal. The extrema occur when the bases of the CIR density compressions, not the direct spot enhancements, are facing the observer (minima in P) and are in the plane of the sky (maxima in P). Fore pole-on ($i = 0°$) views, the magnitude of the polarization does not vary in time, but a circular pattern in the Q-U plane is traversed twice per rotation period. The reasonably strong ($\sim$0.1%) polarization from CIRs here may be conflated with polarization from other sources, e.g., wind compressed disks (see Harries & Howarth 1996). However, most stars exhibiting DACs are thought to be viewed nearly equator-on, and the strongly time-variable polarization computed here can be easily separated from a persistent and non-variable rotational component.

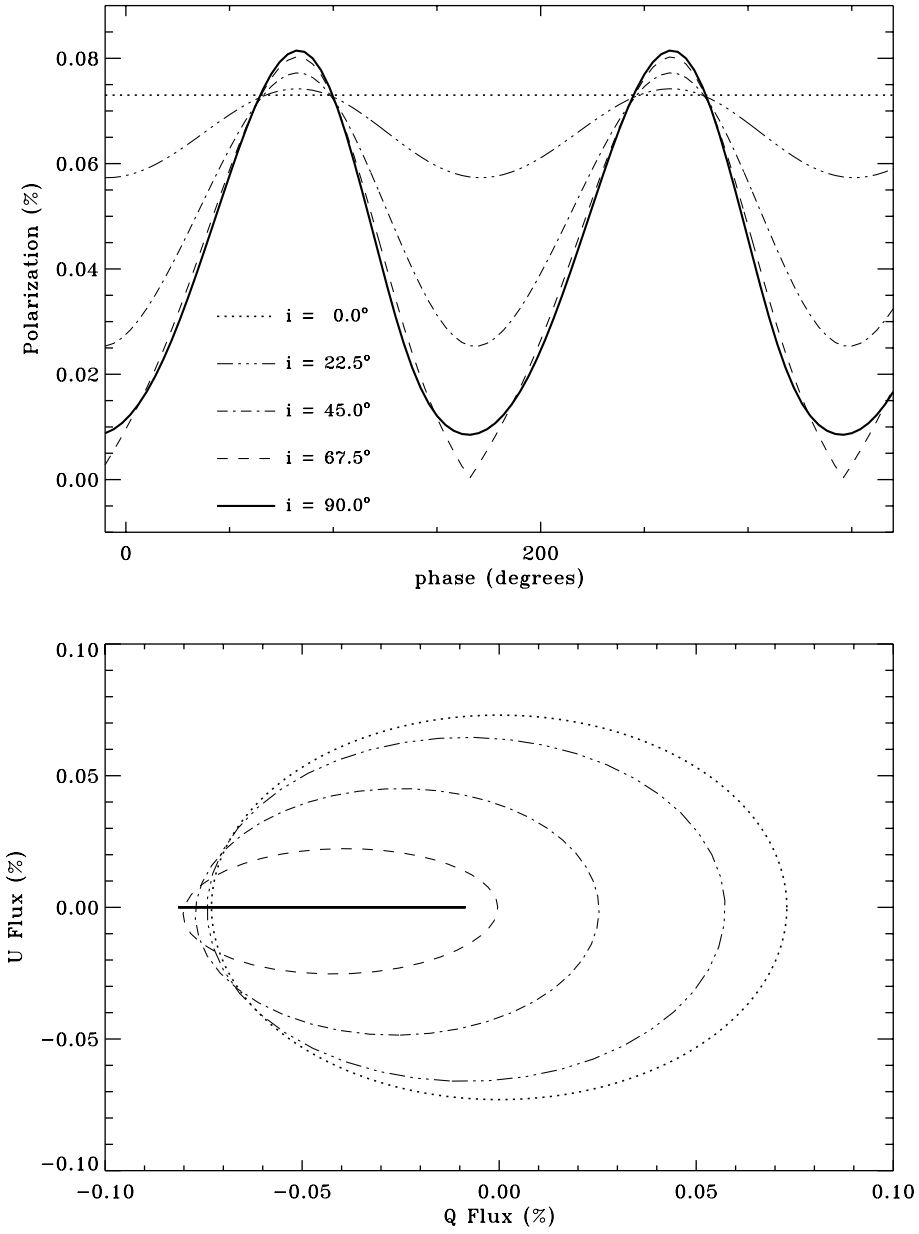

Figure 6.20: The upper plot shows the magnitude of polarization P varying with azimuthal phase, for observers at $i = 0, 22.5, 45, 67.5$, and 90 degrees. The lower plot shows the individual Q and U variations over one full cycle, or 180 degrees of phase.

6.4 Summary, Conclusions, and Future Work

We have carried out two-dimensional hydrodynamical simulations of an azimuthally inhomogeneous radiation-driven wind from a rotating O star. The wind responds to a photospheric radiative force enhancement by forming large-scale corotating structures extending far beyond the region of direct perturbation. Although classical CIR compressions and rarefactions are often seen, the most important structures observationally are slowly-propagating radiative-acoustic kinks or plateaus which have a large Sobolev optical depth. These plateaus show up as strong DACs when formed behind streams resulting from *enhanced mass loss,* and they accelerate at a slower rate than the wind passes through them. Although further calculations will be needed, it seems likely that most possible wind perturbation mechanisms (e.g., localized magnetic "helmet streamers" or steepened nonradial gravo-acoustic oscillations from the photosphere) would also involve similar strong variations in mass flux. Thus, while the spot models computed here may be of limited direct applicability, they provide a useful first basis for analyzing the dynamical and observational characteristics of any such large-scale wind structure associated with mass flux modulations.

Preliminary P Cygni line profile synthesis has shown several important trends in the emergent DACs from these model structures:

1. The slow acceleration of DAC features is fit reasonably well by $\beta \approx 2 - 4$, and we find no significant correlation between their acceleration time scale and the star's rotation velocity. Of course, since the CIRs in our models are linked to the rotating surface, there is a definite correlation between the *recurrence* time scale of DACs and $V_{\rm eq}$.

2. Despite minor variations, the DAC parameters v_c and v_t do not depend strongly on the amplitude A or full width Φ of the model spot perturbation. The primary exception is the high-amplitude Model 3C ($A = 2.50$) which accelerates much more slowly due to the higher density in the CIR shock.

3. The optical depth τ_c and column density N_{col} seem to be sensitive probes of the amplitude of the initial surface perturbation (see Figure 6.16, bottom panel). The concavity of N_{col} during the strongest period of DAC evolution may be able to provide information about the azimuthal size of the perturbation, but this is not as clearly observable an effect (see Figure 6.17, bottom panel).

Let us now compare our model results with actual observations of large-scale wind structure. In many cases both (1) slow and quasi-episodic DACs and (2) faster periodic modulations are seen simultaneously in OB-star winds (Kaper 1993; Massa

et al. 1995). As seen above, the first type of variation can be readily reproduced by the CIR and radiative-acoustic plateau that results from an azimuthally localized mass-loss enhancement. Though our models assume strict rotational periodicity, such DACs could also be readily caused by *transient* CIRs for which the surface mass loss "eruption" lasts long enough to make structure that covers a substantial portion of the stellar disk. The second type of structure observed in OB winds (fast, near-sinusoidal flux variations accelerating *with* the wind) is more difficult to produce with a CIR model, because the required optical depth or density variations disrupt the mean wind velocity streaklines. To explain these faster modulations, we intend to investigate models in which wind structure is induced by nonradial pulsation (NRP) of the underlying star (Owocki, Cranmer, & Fullerton 1995).

The success here in reproducing realistic DACs suggests that the CIR model warrants further study and development. One important extension will be to use a more complete radiative force that incorporates the line-driven instability. The resulting stochastic variations may disrupt the large-scale CIR structure, but slowly evolving kink-like plateaus have been seen to survive and propagate in various one-dimensional instability simulations (Fullerton & Owocki 1992; Owocki, Fullerton, & Puls 1994). In addition, extending the present models to three dimensions may shed light on the variability of wind-compressed disks and other latitudinally-varying structures in, e.g., Be-star winds. Finally, it will be important to develop techniques to synthesize other observational diagnostics, such as subordinate-level ultraviolet and optical lines, infrared photometry, and continuum and line polarization, which will allow further constraints on models of wind variability. The resulting phenomenological "atlas" would provide a solid basis for interpreting the great diversity of OB-star wind variability observations in terms of fundamental, dynamical models of time-dependent wind structure.